

---

# ATTENUATION OF LONG WAVES THROUGH REGIONS OF IRREGULAR FLOATING ICE AND BATHYMETRY

---

A PREPRINT

Lloyd Dafydd & Richard Porter

School of Mathematics, Woodland Road, University of Bristol, Bristol, BS8 1UG, UK

September 12, 2023

## ABSTRACT

Existing theoretical results for attenuation of surface waves propagating on water of random fluctuating depth are shown to over predict the rate of decay due to the way in which ensemble averaging is performed. A revised approach is presented which corrects this and is shown to conserve energy. New theoretical predictions are supported by numerical results which use averaging of simulations of wave scattering over finite sections of random bathymetry for which transfer matrix eigenvalues are used to accurately measure decay. The model of wave propagation used in this paper is derived from a linearised long wavelength assumption whereby depth averaging leads to time harmonic waves being represented as solutions to a simple ordinary differential equation. In this paper it is shown how this can be adapted to incorporate a model of a continuous covering of the surface by fragmented floating ice. Attenuation of waves through broken ice of random thickness is then analysed in a similar manner as bed variations previously and some comparisons are made with published field data for attenuation of waves in the marginal ice zones. Key features of the data are reproduced by theory including the attenuation being proportional to a power of frequency between 2 and 4 as well as capturing the “roll-over effect” at high frequencies.

**Keywords** Wave scattering; Shallow water flows; Sea ice.

## 1 Introduction

It is well known that waves become attenuated as they propagate through an inhomogeneous disordered medium that has randomly varying properties. The term “localisation” is used to describe this phenomenon since the waves are localised in space. Localisation is recognised as a multiple scattering effect caused by incoherent reflections from within the disordered medium and is an energy conserving process; that is, attenuation is not a feature of natural physical dissipative effects.

The pioneering work of Anderson (1958) which first described localisation in quantum systems has since been applied to many other physical systems supporting wave motion. Amongst these, considerable attention has been paid to the propagation of water waves over randomly-varying bathymetry and this is the main initial focus of this paper. Early work in this area considered the randomness be manifested by rectangular steps in the bed. Following the experiments of Belzons *et al.* (1988), Devillard *et al.* (1988) used both shallow water and full potential theory to consider the effect of random stepped bathymetry on wave propagation. Their numerical results supported an asymptotic theory based on a long wavelength assumption that attenuation (the spatial rate of decay and the reciprocal of localisation length) is proportional to the square of the wave frequency. For longer waves, their numerical results based on shallow-water theory diverged, unsurprisingly, from the asymptotic long wavelength theory and from numerical simulations based on full potential theory, and indicated that attenuation tended to a constant for high frequencies. Full potential theory suggested otherwise: that localisation becomes exponentially weak in the short wavelength regime and this was explained as being associated with the exponential decay of wave energy throughout the fluid depth.

Other work on random beds worthy of note include a series of papers by Nachbin and co-authors (see Nachbin & Papanicolaou (1992*a,b*); Nachbin (1995)). Much of the work on waves over random beds have supported the findings

outlined above. Within a linearised setting Mei *et al.* (2005) applies a powerful multiple-scales method (based on the work of Kawahara *et al.* (1976)) for non-shallow potential flow and reaches similar conclusions. The calculation results in an explicit formula for the attenuation rate which is linked to the assumed statistical properties of the bed (now assumed to be defined by a smoothly varying function), as well as wavelength and the mean water depth. Around the same time, a number of papers (see Pihl *et al.* (2002), Grataloup & Mei (2003), Mei & Li (2004)) applied similar multiple-scales analysis to various nonlinear descriptions of wave propagation. In particular Mei & Li (2004) and Grataloup & Mei (2003) considered weakly nonlinear long wavelength theories (Boussinesq approximations). The analytically-derived formulae for wave attenuation differed in that it predicted attenuation increasing like the frequency squared across all frequencies. Thus, there is no levelling off in the attenuation as described by Devillard *et al.* (1988) nor exponential decay as predicted by full potential theory.

More recently, Bennetts *et al.* (2015) returned to the problem of linear full potential theory and performed a series of careful numerical simulations, over stepped beds, which they compared to the theory described by Mei *et al.* (2005). They estimated the attenuation of individual waves, averaged over different realisations of random bathymetry and showed attenuation is significantly weaker than predicted by the theory. They correctly conclude that the ensemble averaging process used in the multiple-scales analysis contributes to an over-prediction of the decay of wave energy due to phase cancellation of propagating waves. Bennetts *et al.* (2015) also attempted to correct for the failings of the existing modelling by including both left- and right-going waves in the leading order solution and by assuming a dependence on the random variables (i.e. stochastic) in the leading order solution, as opposed to making the usual assumption that it is deterministic.

In this paper we revisit the problem of scattering by random bathymetry using a long wavelength/shallow water model which reduces the scattering process to solving an ordinary differential equation (ODE) that includes a coefficient of a random variable with given statistical properties (see Section 3). In particular the random variations in height are considered small compared to the depth. Our analysis (Section 4) is different to previous approaches. First, we assume the randomness occupies a semi-infinite region and define the problem in terms of an incident wave which has the effect of introducing an energy budget. Like Bennetts *et al.* (2015) we include left- and right-propagating waves, but we assume the leading order solution is deterministic. Like Mei *et al.* (2005) (and others) we adopt a multiple-scales approach, but note that the ensemble averaging which determines the attenuation requires careful consideration to remove phase cancellations which are not associated with multiple scattering. In making this correction we also show that energy is conserved.

Theory is compared to numerical simulations which are described in Section 5 of the paper. In Section 6 we use an extension of the model (derived in the Appendix) which allows for the surface of the water to be entirely covered by fragmented ice of variable thickness. The ODE that results differs from the variable bathymetry case only in the definition of three scaling coefficients and a dispersion relation; theory and numerical results are compared in Section 7 of the paper. Also in Section 7, comparisons are made between published field data for attenuation through broken ice taken from a number of studies in polar marginal ice zone regions. These include Wadhams *et al.* (1988), Liu *et al.* (1992), Wadhams *et al.* (2004), Doble *et al.* (2015), Rogers *et al.* (2016), Cheng *et al.* (2017) and Huang & Li (2023). The purpose of this exercise is to demonstrate that some key features in the data such as the relationship between attenuation, frequency and ice thickness as well as the onset of high-frequency “roll-over” are all capable of being captured by this basic theoretical model of attenuation through broken ice. This is significant since there are no current physically-motivated models which describe these features; see discussions in Montiel *et al.* (2022), Meylan *et al.* (2018). In the latter reference, ad-hoc models of damping (including the widely-cited “Robinson-Palmer model”) are incorporated into dynamic boundary conditions at the water surface which lead to attenuation with a power law dependence which falls within the range of field observations. Notably, however, our model suggests that randomness and localisation, not physical dissipation, is a possible mechanism for attenuation. Finally, the work is summarised in Section 8.

## 2 Summary of the model

We consider a two-dimensional scattering problem in which plane-crested monochromatic waves of small amplitude propagate in the positive  $x$ -direction in  $x < 0$  over fluid of constant depth with a surface covered by a continuous layer fragmented ice of constant thickness. There are no physical mechanisms included in the model for energy dissipation such as fluid viscosity or ice-ice friction. Incident wave energy is partially reflected from, and partially transmitted into, the region  $x > 0$ . This is due to either randomly-varying bathymetry or by randomly-varying thickness of broken ice (both are illustrated in Fig. 1) which extends over the interval  $0 < x < L$  before returning, in  $x > L$ , to the same constant values found in  $x < 0$ . We are interested in monitoring the reflected and transmitted wave energy. In Section 4 we set  $L = \infty$  so that the randomness extends indefinitely into  $x > 0$ . In this case all incoming wave energy will be reflected and the focus is determining the attenuation of waves as a function of distance into  $x > 0$ .

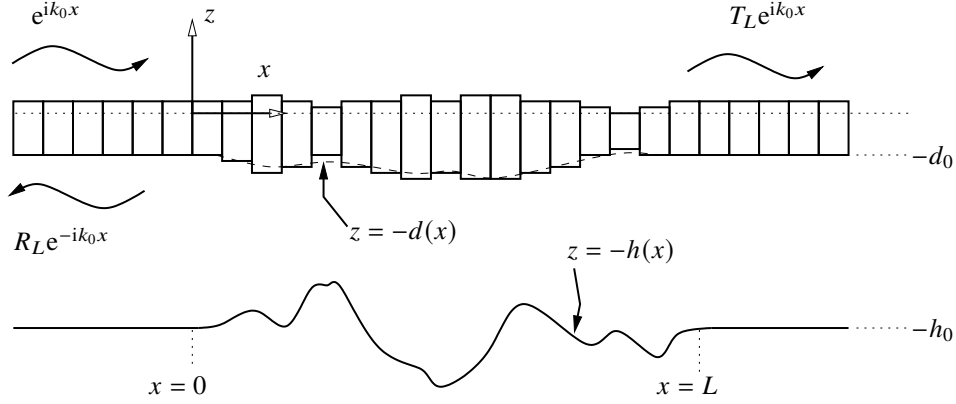


Figure 1: Definition sketch of variable floating broken ice over a variable bed.

Porter (2019) developed a shallow-water (long wavelength) model for wave scattering over variable bathymetry with no ice cover. This model results from an expansion to second order in a small parameter representing the ratio of vertical to horizontal lengthscales combined with depth averaging and is expressed by

$$(\hat{h}(x)\Omega'(x))' + K\Omega(x) = 0 \quad (1)$$

where  $K = \omega^2/g$ ,  $\omega$  is the angular frequency of the motion,  $g$  represents gravitational acceleration and

$$\hat{h}(x) = \frac{h(x)(1 - \frac{1}{3}Kh(x))}{1 + \frac{1}{3}v(h)h'^2(x)} \quad (2)$$

is defined in terms of the fluid depth  $h(x)$ . Here,  $v(h) = 1 + \frac{1}{12}Kh(x)/(1 - \frac{1}{3}Kh(x))$  and  $v(h) \approx 1$  is a simplification which will be adopted hereafter. The underlying assumptions are expressed by the formal constraint that  $Kh \ll 1$ , although Porter (2019) showed by comparing with exact results for reflected and transmitted wave energy for shoaling beds of finite length, that the model produces accurate predictions up to  $Kh \approx 1$ .

The dependent variable,  $\Omega$ , in (1) is related to the time-dependent wave elevation  $\zeta(x, t) = \Re\{\eta(x)e^{-i\omega t}\}$  by

$$\eta(x) = \frac{-i/\omega}{\sqrt{1 - \frac{1}{3}Kh(x)}} \left( \Omega(x) - \frac{\frac{1}{6}hh'}{1 + \frac{1}{3}h'^2} \Omega'(x) \right). \quad (3)$$

It was shown in Porter (2019) that  $\Omega(x)$  and  $\Omega'(x)$  remain continuous at discontinuities in  $h'(x)$ .

Porter (2019) highlighted the significant improvement in results away from the zero frequency limit that could be achieved when  $\hat{h}(x) = h(x)$  is replaced by the definition in (2), applying in the case of the standard linear shallow water equation. Thus, the modification in (2) includes, in the numerator, the effect of weak dispersion and, in the denominator, a geometric factor indicating a reduction in wave speed over sloping beds. We also remark that (1) can also be derived from a linearisation of Boussinesq equations (e.g. Peregrine (1967)) whereby wave amplitudes are assumed sufficiently small compared to  $Kh$ .

In the Appendix, the model developed by Porter (2019) is extended to include the additional effect of a floating fragmented ice cover. Additional assumptions apply here. Ice is assumed to completely cover the surface of the fluid and is broken into sections which are sufficiently small in horizontal extent and whose thickness varies slowly enough that the submergence of the ice is represented by a continuous function,  $d(x)$ . The motion of the ice is constrained in heave (vertical) motion and the expansion to second-order the depth ratio ( $\epsilon$  in the Appendix) in the modelling is needed to include the effect of inertia of floating ice. That is, a basic first-order linear shallow-water model neglects vertical accelerations and the effect of ice cover at leading order is manifested only through a reduction in the depth of the fluid from  $h(x)$  to  $h(x) - d(x)$ . Thus, our second-order model extended to incorporate floating ice of submergence  $d(x)$  is, see (A.38),

$$(\hat{d}(x)\Omega'(x))' + K\Omega(x) = 0, \quad (4)$$

where  $\hat{d}(x)$  is defined by (A.39) and the free surface elevation is related to  $\Omega$  by (A.40). As before,  $\Omega$  and  $\Omega'$  are continuous even if  $d'(x)$  and/or  $h'(x)$  is discontinuous.

In  $x < 0$  and in  $x > L$  we assume  $h = h_0$ ,  $d = d_0$  are both constant. Then (4) can be solved explicitly and

$$\Omega(x) = e^{ik_0x} + R_L e^{ik_0x}, \quad x < 0 \quad (5)$$

$$\Omega(x) = T_L e^{ik_0x}, \quad x > L \quad (6)$$

where  $R_L$  and  $T_L$  are reflection and transmission coefficients, satisfying  $|R_L|^2 + |T_L|^2 = 1$  (energy conservation) and

$$k_0^2(h_0 - d_0) = \frac{K}{1 - \frac{1}{3}K(h_0 + 2d_0)} \quad (7)$$

defines the wavenumber,  $k_0$ , in terms of the frequency  $\omega$ . This shallow water dispersion relation is weakly dispersive, but for sufficiently small frequencies we note that  $k_0 \propto \omega$ .

### 3 Description of randomness

We will consider wave propagation over a region  $0 < x < L$  in which either the bed or the ice thickness randomly varies. We could consider both simultaneously varying, but for clarity consider the two effects separately.

We say that either

$$d = 0, \quad h(x) = h_0(1 + \sigma r(x)) \quad (8)$$

or that

$$h = h_0, \quad d(x) = d_0(1 + \sigma r(x)) \quad (9)$$

such that  $r(x)$  is a random function with mean zero and unit variance. That is

$$\langle r \rangle = 0, \quad \langle r^2 \rangle = 1, \quad (10)$$

implying that  $\sigma$  is the RMS of the vertical variations of  $h(x)$  or  $d(x)$ . We ensure that the  $r(0) = r'(0) = r(L) = r'(L) = 0$  so that the bed/ice thickness joins the constant values in  $x < 0$  and  $x > L$  smoothly. The random function  $r(x)$  also satisfies the Gaussian correlation relation

$$\langle r(x)r(x') \rangle = e^{-|x-x'|^2/\Lambda^2} \quad (11)$$

(other models have used an exponential correlation function, but show that it produces only small differences in results). Thus,  $\Lambda$  characterises the horizontal lengthscale of the random bed fluctuations.

### 4 Analysis of the model

In this section, we assume  $L \rightarrow \infty$  so that the randomness occupies  $x > 0$ . The main assumption that is made is that the amplitude of the randomness is small, i.e.  $\sigma \ll 1$ . We note that we can write (4) with (A.39), (A.41) and either (8) or (9) as

$$((1 + \sigma C_1 r(x) - \sigma^2(C_2 r^2(x) + C_3 r'^2(x)))\Omega')' + k_0^2 \Omega = 0, \quad x > 0 \quad (12)$$

where terms up to  $O(\sigma^2)$  have been retained, and

$$\Omega'' + k_0^2 \Omega = 0, \quad x < 0 \quad (13)$$

where  $k_0$  is defined by (7). In (12), the coefficients depend on the whether the bed or the thickness of floating ice is represented by the random function  $r(x)$ . In the case that the bed is varying and the ice is absent,  $d_0 = 0$  and

$$C_1 = \frac{1 - \frac{2}{3}Kh_0}{1 - \frac{1}{3}Kh_0}, \quad C_2 = \frac{\frac{1}{3}Kh_0}{1 - \frac{1}{3}Kh_0}, \quad C_3 = \frac{1}{3}h_0^2 \quad (14)$$

and in the case where the ice is varying and the bed is of constant depth,  $h(x) = h_0$  and

$$C_1 = \frac{-d_0(1 + \frac{1}{3}K(h_0 - 4d_0))}{(h_0 - d_0)(1 - \frac{1}{3}K(h_0 + 2d_0))}, \quad C_2 = \frac{-\frac{2}{3}Kd_0^2}{(h_0 - d_0)(1 - \frac{1}{3}K(h_0 + 2d_0))}, \quad C_3 = \frac{1}{3}d_0^2. \quad (15)$$

The long wave assumption on which the model is based formally requires  $Kd_0 < Kh_0 \ll 1$  and so we do not envisage using the model close to  $Kh_0 = 3$  or  $K(h_0 + 2d_0) = 3$ . The solution to (13) is

$$\Omega(x) = e^{ik_0x} + R_\infty e^{-ik_0x} \quad (16)$$

and since we anticipate decay of waves into  $x \rightarrow \infty$  we also impose  $\Omega \rightarrow 0$  as  $x \rightarrow \infty$  and so we must require that  $|R_\infty| = 1$ ; all incident wave energy is reflected.

We make the multiple scales assumption of, for e.g., Mei & Li (2004) (but also see other references listed in the introduction) and introduce a slow variable  $X = \sigma^2 x$ , writing

$$\Omega(x) = \Omega_0(x, X) + \sigma \Omega_1(x, X) + \sigma^2 \Omega_2(x, X) + \dots \quad (17)$$

Accordingly (12) becomes

$$\left[ \left( \frac{\partial}{\partial x} + \sigma^2 \frac{\partial}{\partial X} \right) \left( \left( 1 + \sigma C_1 r(x) - \sigma^2 (C_2 r^2(x) + C_3 r'^2(x)) \right) \left( \frac{\partial}{\partial x} + \sigma^2 \frac{\partial}{\partial X} \right) \right) + k_0^2 \right] (\Omega_0 + \sigma \Omega_1 + \sigma^2 \Omega_2 + \dots) = 0, \quad x > 0. \quad (18)$$

The matching conditions at  $x = 0$  consist of

$$\Omega(0^-) = 1 + R_\infty = \left( \Omega_0 + \sigma \Omega_1 + \sigma^2 \Omega_2 + \dots \right)_{x=X=0} \quad (19)$$

and

$$\Omega'(0^-) = ik_0(1 - R_\infty) = \left( \frac{\partial}{\partial x} + \sigma^2 \frac{\partial}{\partial X} \right) (\Omega_0 + \sigma \Omega_1 + \sigma^2 \Omega_2 + \dots)_{x=X=0}. \quad (20)$$

At leading order,  $\Omega_0$  satisfies the same wave equation (13) as in  $x < 0$  and its general solution is

$$\Omega_0(x, X) = A(X)e^{ik_0 x} + B(X)e^{-ik_0 x}. \quad (21)$$

This implies that the leading order solution is not explicitly dependent on individual realisations,  $r(x)$ ;  $A$  and  $B$  will contain information relating to the statistical properties of  $r(x)$  however. We require that long-scale variations,  $A(X)$  and  $B(X)$ , to tend to zero as  $X \rightarrow \infty$ , whilst  $A(0) = 1$  and  $B(0) = R_\infty$  are determined from the matching conditions (19), (20) at leading order.

Since  $|R_\infty| = 1$  there must be no net time-averaged transport of energy flux in  $x > 0$  and so we expect that

$$|A(X)| = |B(X)|. \quad (22)$$

At  $O(\sigma)$  we have

$$\frac{\partial^2 \Omega_1}{\partial x^2} + k_0^2 \Omega_1 = -C_1 \frac{\partial}{\partial x} \left( r(x) \frac{\partial \Omega_0}{\partial x} \right). \quad (23)$$

Its solution can be determined using the Green's function for the one-dimensional wave equation,

$$g(x, x') = \frac{e^{ik_0|x-x'|}}{2ik_0}, \quad (24)$$

satisfying

$$\frac{\partial^2}{\partial x^2} g + k_0^2 g = \delta(x - x'), \quad (25)$$

and outgoing as  $|x - x'| \rightarrow \infty$ . The right-hand side of (23) is comprised of two terms forced by right- and left-propagating waves and the solution  $\Omega_1$ , in  $x > 0$ , is a superposition of solutions derived using  $g$  and  $\bar{g}$ , respectively, in Green's identity with the two components of  $\Omega_1$  over  $x > 0$  and results in

$$\Omega_1(x, X) = -ik_0 C_1 A(X) \int_0^\infty g(x, x') \frac{\partial}{\partial x'} \left( r(x') e^{ik_0 x'} \right) dx' + ik_0 C_1 B(X) \int_0^\infty \bar{g}(x, x') \frac{\partial}{\partial x'} \left( r(x') e^{-ik_0 x'} \right) dx', \quad x > 0. \quad (26)$$

The use of  $\bar{g}$  is non-standard and implies that the component of the first-order solution associated with left-propagating leading-order wave is represented by a distribution of incoming waves. This is required to satisfy the energy balance equation (22). Put another way, we require the amplitude,  $B(X)$ , of the left-going wave to grow as it propagates from right to left, its associated energy being generated from the energy lost to outgoing waves from the right-propagating wave with amplitude  $A(X)$ .

Integrating by parts once, using  $r(0) = 0$  (since the random variations in the bed or the ice continuously joins the constant value set in  $x < 0$ ) gives

$$\begin{aligned} \Omega_1(x, X) = & -ik_0 C_1 A(X) \int_0^\infty \frac{\partial}{\partial x} g(x, x') r(x') e^{ik_0 x'} dx' \\ & + ik_0 C_1 B(X) \int_0^\infty \frac{\partial}{\partial x} \bar{g}(x, x') r(x') e^{-ik_0 x'} dx'. \end{aligned} \quad (27)$$

Here  $\partial_x g = -\partial_{x'} g$  has been used and we note that this function is discontinuous at  $x = x'$ .

We also remark that  $\Omega_1$  is a random function with zero mean since  $\langle \Omega_1 \rangle = 0$  follows from ensemble averaging (27) and using (10).

At  $O(\sigma^2)$  we have

$$\frac{\partial^2 \Omega_2}{\partial x^2} + k_0^2 \Omega_2 = -C_1 \frac{\partial}{\partial x} \left( r(x) \frac{\partial \Omega_1}{\partial x} \right) - 2 \frac{\partial^2 \Omega_0}{\partial x \partial X} + \frac{\partial}{\partial x} \left( (C_2 r^2(x) + C_3 r'^2(x)) \frac{\partial \Omega_0}{\partial x} \right). \quad (28)$$

We ensemble average the equation using the results from (10) and  $\langle r'^2 \rangle = 2/\Lambda^2$  (this can be established using the definition of the derivative as a limit) to give

$$\begin{aligned} \frac{\partial^2}{\partial x^2} \langle \Omega_2 \rangle + k_0^2 \langle \Omega_2 \rangle = & -C_1 \frac{\partial}{\partial x} \left\langle r(x) \frac{\partial \Omega_1}{\partial x} \right\rangle - 2ik_0 (A'(X) e^{ik_0 x} - B'(X) e^{-ik_0 x}) \\ & - k_0^2 (C_2 + 2C_3/\Lambda^2) (A(X) e^{ik_0 x} + B(X) e^{-ik_0 x}). \end{aligned} \quad (29)$$

It is instructive to write  $\Omega_1$  from (27) in terms of separate wave-like components as

$$\begin{aligned} \Omega_1(x, X) = & -\frac{C_1 A(X) ik_0}{2} \left[ e^{ik_0 x} \int_0^x r(x') dx' - e^{-ik_0 x} \int_x^\infty r(x') e^{2ik_0 x'} dx' \right] \\ & + \frac{C_1 B(X) ik_0}{2} \left[ e^{-ik_0 x} \int_0^x r(x') dx' - e^{ik_0 x} \int_x^\infty r(x') e^{-2ik_0 x'} dx' \right]. \end{aligned} \quad (30)$$

We note that the leading-order right-propagating wave excites both right-propagating waves which accumulate from interactions with the bed to the left of the observation point,  $x$ , and left-propagating waves which represent the accumulation of upwave reflections from bed interactions to the right of the observation point. Similar comments apply to terms proportional to the leading-order left-propagating wave. The ensemble averaging of the first and third terms of (30) in (29) lead to a contribution to the attenuation which we describe as ‘‘fictitious decay’’. That is to say, it is a feature of wave scattering not experienced by individual waves, but which instead originates from phase cancellations from first-order waves when averaged over realisations of  $r(x)$ : phases are not altered by the choice of  $r(x)$ . For the purpose of computing the attenuation experienced by individual waves we remove this fictitious decay effect, replacing (30) by

$$\Omega_1(x, X) = \frac{C_1 A(X) ik_0}{2} e^{-ik_0 x} \int_x^\infty r(x') e^{2ik_0 x'} dx' - \frac{C_1 B(X) ik_0}{2} e^{ik_0 x} \int_x^\infty r(x') e^{-2ik_0 x'} dx'. \quad (31)$$

The only term requiring attention now is the first term on the right-hand side of (29) where  $\Omega_1$  is given by (31). It is straightforward to determine from (31) that

$$\begin{aligned} \left\langle r(x) \frac{\partial \Omega_1}{\partial x} \right\rangle = & -\frac{ik_0}{2} C_1 A(X) e^{ik_0 x} + k_0^2 C_1 A(X) e^{ik_0 x} \int_0^\infty e^{-\xi^2/\Lambda^2} e^{2ik_0 \xi} d\xi \\ & + \frac{ik_0}{2} C_1 B(X) e^{-ik_0 x} + k_0^2 C_1 B(X) e^{-ik_0 x} \int_0^\infty e^{-\xi^2/\Lambda^2} e^{-2ik_0 \xi} d\xi \end{aligned} \quad (32)$$

after using the definition in (11) and making a substitution  $\xi = x - x'$ . As demanded by (29), we need to take a further derivative which results in

$$C_1 \frac{\partial}{\partial x} \left\langle r(x) \frac{\partial \Omega_1}{\partial x} \right\rangle = \frac{C_1^2 k_0^2}{2} (A(X) F e^{ik_0 x} + B(X) \bar{F} e^{-ik_0 x}) \quad (33)$$

where

$$F = 1 + ik_0 \int_0^\infty e^{-\xi^2/\Lambda^2} e^{2ik_0 \xi} d\xi = 1 + \frac{\sqrt{\pi}}{2} ik_0 \Lambda e^{-k_0^2 \Lambda^2} (1 + i \operatorname{erfi}(k_0 \Lambda)), \quad (34)$$

(see, e.g., Mei & Li (2004)) and  $\text{erfi}(\cdot)$  is the imaginary error function.

Armed with (34), we return to the governing equation (29) for  $\langle \Omega_2 \rangle$  and note that the right-hand side contains secular terms; that is functions proportional to  $e^{\pm ik_0 x}$ . These must be removed to avoid unbounded growth in the solution for  $\langle \Omega_2 \rangle$  as  $x \rightarrow \infty$ . In doing so we obtain

$$\frac{\partial^2}{\partial x^2} \langle \Omega_2 \rangle + k_0^2 \langle \Omega_2 \rangle = 0, \quad (35)$$

whilst  $A(X)$  and  $B(X)$  satisfy

$$2ik_0 A'(X) = -k_0^2 A(X) \left( C_1^2 \left( \frac{1}{2} + \frac{\sqrt{\pi}}{4} ik_0 \Lambda e^{-k_0^2 \Lambda^2} (1 + i \text{erfi}(k_0 \Lambda)) \right) + C_2 + 2C_3/\Lambda^2 \right) \quad (36)$$

and

$$-2ik_0 B'(X) = -k_0^2 B(X) \left( C_1^2 \left( \frac{1}{2} - \frac{\sqrt{\pi}}{4} ik_0 \Lambda e^{-k_0^2 \Lambda^2} (1 - i \text{erfi}(k_0 \Lambda)) \right) + C_2 + 2C_3/\Lambda^2 \right). \quad (37)$$

Solving for  $A(X)$  with  $A(0) = 1$  gives

$$A(X) = e^{-QX + i\kappa X} \quad (38)$$

where

$$Q = \frac{\sqrt{\pi}}{8} C_1^2 k_0^2 \Lambda e^{-k_0^2 \Lambda^2} \quad (39)$$

and

$$\kappa = C_1^2 \left( \frac{k_0}{4} - \frac{\sqrt{\pi}}{8} k_0^2 \Lambda e^{-k_0^2 \Lambda^2} \text{erfi}(k_0 \Lambda) \right) + k_0 C_2/2 + k_0 C_3/\Lambda^2. \quad (40)$$

Meanwhile, solving (37) for  $B(X)$  with  $B(0) = R_\infty$  such that  $|R_\infty| = 1$  gives

$$B(X) = R_\infty e^{-QX - i\kappa X} \quad (41)$$

and thus (27) is satisfied.

Had the first and third terms in (30) not been removed and (30) not been replaced by (31) then, amongst other changes, the expression in (39) would have been replaced by  $Q = (\sqrt{\pi}/8) C_1^2 k_0^2 \Lambda (1 + e^{-k_0^2 \Lambda^2})$ . A similar attenuation factor is determined in the work of Mei *et al.* (2005) and Bennetts *et al.* (2015). The additional factor of +1, associated with phase cancellation in the ensemble averaging, completely changes the character of attenuation. Bennetts *et al.* (2015) highlight the discrepancy between theoretical results and attenuation measured through discrete numerical simulations, most notably in Figures 5 and 6 of their paper. Moreover, the expression for  $B(X)$  would also change with the factor of  $Q$  associated with (41) replaced by  $Q = (\sqrt{\pi}/8) C_1^2 k_0^2 \Lambda (-1 + e^{-k_0^2 \Lambda^2})$  implying exponential growth towards infinity of the left-propagating wave whilst (27) is no longer satisfied.

Returning to (21) gives the leading order solution in  $x > 0$  as

$$\Omega(x) \approx \Omega_0(x, \sigma^2 x) = e^{-\sigma^2 Q x} \left( e^{i(k_0 + \sigma^2 \kappa)x} + R_\infty e^{-i(k_0 + \sigma^2 \kappa)x} \right). \quad (42)$$

Furthermore, since  $\langle \Omega_1 \rangle = 0$ , corrections to (42) are  $O(\sigma^2)$ . From (42) the attenuation rate is defined to be

$$k_i = \sigma^2 Q = \frac{\sqrt{\pi}}{8} k_0^2 \sigma^2 \Lambda C_1^2 e^{-k_0^2 \Lambda^2} \quad (43)$$

with  $C_1$  given by (14) (or (15)), a factor which depends upon  $k_0 h_0$  (and  $d_0/h_0$ ). In the case of a randomly-varying bed with no ice cover and assuming  $C_1^2 \approx 1$  since  $Kh_0 \ll 1$ , the maximum value of  $k_i$  will occur at  $k_0 \Lambda \approx 1$ . This value can be interpreted as being associated with Bragg resonance which occurs close to  $k_0 \Lambda = 1$  for periodic beds with periodicity  $\Lambda$ . Bragg resonance is characterised by coherent multiple reflections. In the case of varying ice  $C_1^2 \approx d_0^2/(h_0 - d_0)^2$  which alters the magnitude of the attenuation, but not the condition  $k_0 \Lambda \approx 1$  for the maximum.

For  $k_0 \Lambda \ll 1$ ,  $k_i \propto k_0^2$  whilst for  $k_0 \Lambda \gg 1$  the attenuation decays exponentially as  $k_0 \Lambda$  increases. The latter result holds in this long wavelength model and contrasts with the conclusions drawn by previous researchers (e.g. see Devillard *et al.* (1988), Mei *et al.* (2005)) who associate exponential decay in wave attenuation as a finite water depth effect.

These conclusions are based on a long wave model of wave propagation with randomness described by a continuously varying function. For short wave scattering by floating broken ice, for example, the physics will be different as scattering by discrete ice floes will need to be correctly modelled.

## 5 Numerical methods and simulations

### 5.1 Generating a random surface

In order to numerically generate a random function,  $r(x)$ , with statistical properties (10) and (11) characterised by the RMS height 1 and the correlation length  $\Lambda$  we implement the weighted moving average method described in Sarris *et al.* (2021) and originally due to Ogilvy (1988). The function  $r(x)$  will be defined at  $x = x_i = i\Delta x$  for  $i = 0, \dots, V$  where  $\Delta x = L/V$ ; either  $\Delta x$  or  $V$  can be used as the numerical parameter defining the resolution of the random surface.

We generate the Gaussian weights

$$w_j = W e^{-2(j\Delta x)^2/\Lambda^2} \quad (44)$$

for  $j = -M, \dots, M$  where  $M = \lfloor 4\Lambda/(\Delta x\sqrt{2}) \rfloor$  (denoting integer part) is a truncation parameter and  $W$  is defined to normalise these values so that

$$\sum_{j=-M}^M w_j = 1. \quad (45)$$

Next, we define

$$\sigma_v^2 = 1 / \sum_{j=-M}^M w_j^2 \quad (46)$$

which is used to generate the  $2N + 1$  uncorrelated random numbers  $v_i$ ,  $-N \leq i \leq N$  from a Gaussian distribution with a variance of  $\sigma_v$ . The height of a random surface at  $x = x_i$  is defined by

$$r_i = \sum_{j=-M}^M w_j v_{j+i+M-N}, \quad i = 0, \dots, V \quad (47)$$

requiring  $N$  to be defined by  $2N = V + 2M$ . Our theory requires that  $r(x) = 0$  at  $x = 0, x = L$  and that these values to approached smoothly from within the interval  $x \in (0, L)$ . We thus introduce a Tukey smoothing window at either end of the interval of length  $\Lambda$  (assumed to be less than  $L/2$ ) via

$$r(x_i) = \begin{cases} r_i, & V_\Lambda + 1 \leq i \leq V - V_\Lambda - 1, \\ r_i \left( \frac{1}{2} - \frac{1}{2} \cos \left( \frac{i\pi}{V_\Lambda} \right) \right), & i = 0, \dots, V_\Lambda, \\ r_i \left( \frac{1}{2} - \frac{1}{2} \cos \left( \pi \frac{V-i}{V_\Lambda} \right) \right), & i = V - V_\Lambda, \dots, V, \end{cases} \quad (48)$$

where  $V_\Lambda = \lfloor \Lambda/\Delta x \rfloor$ . Numerically, we ensure  $V_\Lambda$ , which represents the number of points per characteristic length of bed, is sufficiently large.

### 5.2 Determining decay via a transfer matrix

Simulations of scattering are performed over a region  $0 < x < L$  with  $L/h_0 \gg 1$ . Taking  $L$  to be large is done since we wish to compare are results with the theoretical results where  $L = \infty$ . Thus, we aim to ensure that waves pass over enough of the bed for the effect of randomness to be felt. Attenuation over longer beds can also help suppress multiple scattering effects associated with the junctions at  $x = 0$  and  $x = L$  between constant and random surfaces. However, the method described below for determining attenuation is insensitive to multiple scattering effects.

Instead of (5), (6), let us momentarily express the solution in  $x < 0, x > L$  more generally as

$$\Omega(x) = \begin{cases} A_- e^{ik_0 x} + B_- e^{-ik_0 x}, & x < 0 \\ A_+ e^{ik_0 x} + B_+ e^{-ik_0 x}, & x > L \end{cases} \quad (49)$$

for complex constants  $A_\pm, B_\pm$ , representing amplitudes of right- and left-propagating waves, respectively, whilst  $k_0$  satisfies (7).

We encode scattering using either a  $2 \times 2$  scattering matrix,  $\mathbf{S}$ , satisfying

$$\begin{pmatrix} A_+ \\ B_- \end{pmatrix} = \mathbf{S} \begin{pmatrix} A_- \\ B_+ \end{pmatrix} \quad (50)$$

which relates outgoing to incoming waves or a  $2 \times 2$  transfer matrix,  $\mathbf{P}$ , satisfying

$$\begin{pmatrix} A_+ \\ B_+ \end{pmatrix} = \mathbf{P} \begin{pmatrix} A_- \\ B_- \end{pmatrix} \quad (51)$$

which relates waves in  $x > L$  to waves in  $x < 0$ . Energy conservation requires incoming and outgoing wave energy fluxes balance so that  $|A_-|^2 + |B_+|^2 = |A_+|^2 + |B_-|^2$  and this implies  $\overline{\mathbf{S}}^T \mathbf{S} = \mathbf{I}$  where  $\mathbf{I}$  is the Identity and the overbar denotes conjugation;  $\mathbf{S}$  is a unitary matrix. Multiplying (51) by  $(\overline{A_+}, -\overline{B_+})^T$  results in a similar identity

$$\mathbf{E} \overline{\mathbf{P}}^T \mathbf{E} \mathbf{P} = \mathbf{I}, \quad \mathbf{E} = \begin{pmatrix} 1 & 0 \\ 0 & -1 \end{pmatrix}. \quad (52)$$

This is sufficient to show that if  $\lambda$  is an eigenvalue of  $\mathbf{P}$  then so is  $\overline{\lambda}$ , as is  $1/\overline{\lambda}$ . The pair of eigenvalues  $\lambda_{\pm}$  of  $\mathbf{P}$  are therefore either both real, occurring in reciprocal pairs, or complex conjugates lying on the unit circle.

As shown in, for example Porter & Porter (2003), the eigenvalues characterise wave propagation across  $0 < x < L$ : if  $\lambda_{\pm}$  are complex conjugates then there is no attenuation as waves travel from left to right. If, however,  $\lambda_{\pm}$  are real, then writing  $\lambda_+ = e^{-k_i L}$  and  $\lambda_- = e^{k_i L}$ , say, indicate that right- and left-propagating waves are attenuated with the rate  $k_i$ .

Since the transfer matrix,  $\mathbf{P}$ , describes the solution over  $0 < x < L$  without coupling to the solution in  $x < 0$  and  $x > L$  its eigenvalues determine decay (or otherwise) without interference from multiple scattering effects associated with waves being reflected at the junctions  $x = 0$  and  $x = L$ .

The entries of  $\mathbf{S}$  and  $\mathbf{P}$  requires us to solve (4). We follow Porter (2019), write  $x = \xi L$  and numerically solve the dimensionless coupled first order system

$$p'_i(\xi) = (L/\hat{d}(L\xi))q_i(\xi), \quad q'_i(\xi) = -KLp_i(\xi), \quad 0 < \xi < 1 \quad (53)$$

for  $i = 1, 2$  with the initial conditions  $p_1(0) = 1$ ,  $q_1(0) = 0$  and  $p_2(0) = 0$  and  $q_2(0) = 1$ . This allows us, after matching to the solution given by (49) in  $x < 0$  and  $x > L$  and with some manipulation of the algebra, to express the solution either using (50) with

$$\mathbf{S} = \begin{pmatrix} i(K/k_0)p_2(1) - p_1(1) & e^{ik_0L} \\ i(K/k_0)q_2(1) - q_1(1) & i(K/k_0)e^{ik_0L} \end{pmatrix}^{-1} \begin{pmatrix} i(K/k_0)p_2(1) + p_1(1) & e^{-ik_0L} \\ i(K/k_0)q_2(1) + q_1(1) & -i(K/k_0)e^{-ik_0L} \end{pmatrix} \quad (54)$$

or using (51) with

$$\mathbf{P} = \begin{pmatrix} e^{ik_0L} & e^{-ik_0L} \\ i(K/k_0)e^{ik_0L} & -i(K/k_0)e^{-ik_0L} \end{pmatrix}^{-1} \begin{pmatrix} i(K/k_0)p_2(1) + p_1(1) & -i(K/k_0)p_2(1) + p_1(1) \\ i(K/k_0)q_2(1) + q_1(1) & -i(K/k_0)q_2(1) + q_1(1) \end{pmatrix}. \quad (55)$$

When we set  $A_- = 1$  and  $B_+ = 0$ ,  $B_- = R_L$  and  $A_+ = T_L$  become the reflection and transmission coefficients to due waves incident from  $x < 0$  which are most easily determined from (50) with (54).

Attenuation, on the other hand, simply requires us to evaluate the pair of eigenvalues of  $\mathbf{P}$  from (55). The corresponding decay rate is then determined from  $k_i = |\ln |\lambda_+||/L$  which, in the case of complex conjugate eigenvalues is zero.

For the ensemble averaging the results we run  $N \gg 1$  simulations of different randomisations of the bed or the ice thickness and then compute

$$\langle k_i \rangle = \frac{1}{N} \sum_{n=1}^N k_i, \quad \langle |R_L| \rangle = \frac{1}{N} \sum_{n=1}^N |R_L|, \quad \langle |T_L| \rangle = \frac{1}{N} \sum_{n=1}^N |T_L|, \quad (56)$$

where the terms under the sum represent the output of each random simulation. Depending on numerical parameters used, computations of the three averages will typically take between 20 and 200 seconds on a standard desktop PC when  $N = 500$ . A standard Runge-Kutta 4.5 method is used to solve (53).

## 6 Results for randomly varying beds without ice cover

We start by illustrating the numerical solution from a single realisation of a random bed. In Fig. 2 the function  $h(x)/h_0$  is plotted about -2 on the vertical scale in the figure which is used to represent the real and imaginary parts of the wave elevation. In this simulation the bed is defined by  $\Lambda = 2h_0$ ,  $\sigma^2 = 0.02$  and  $L = 400h_0$ . The figure illustrates the randomness of the wave response over the bed and partial reflection and transmission of the incident wave. Note that partial transmission is not necessarily a result of wave attenuation over the random bed and occurs whenever there are

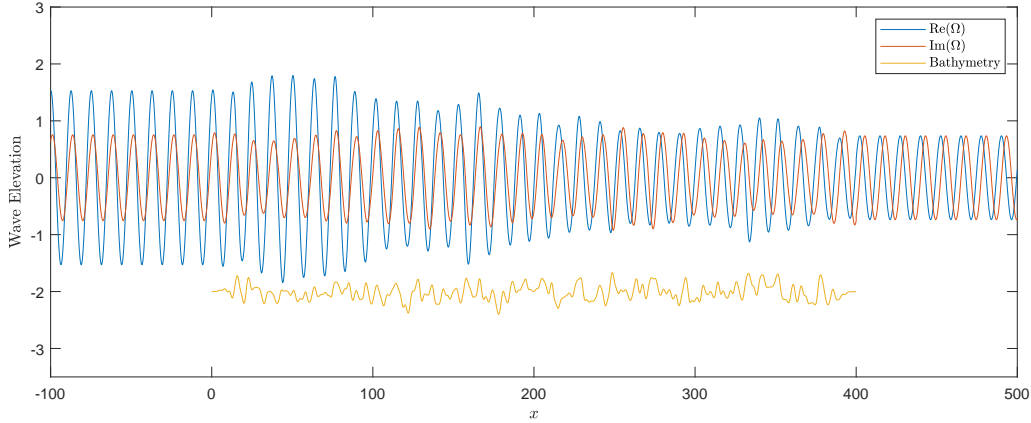


Figure 2: An example wave form corresponding to a randomly generated bed with  $\sigma^2 = 0.02$ ,  $\Lambda = 2h_0$  and  $L = 400h_0$ .

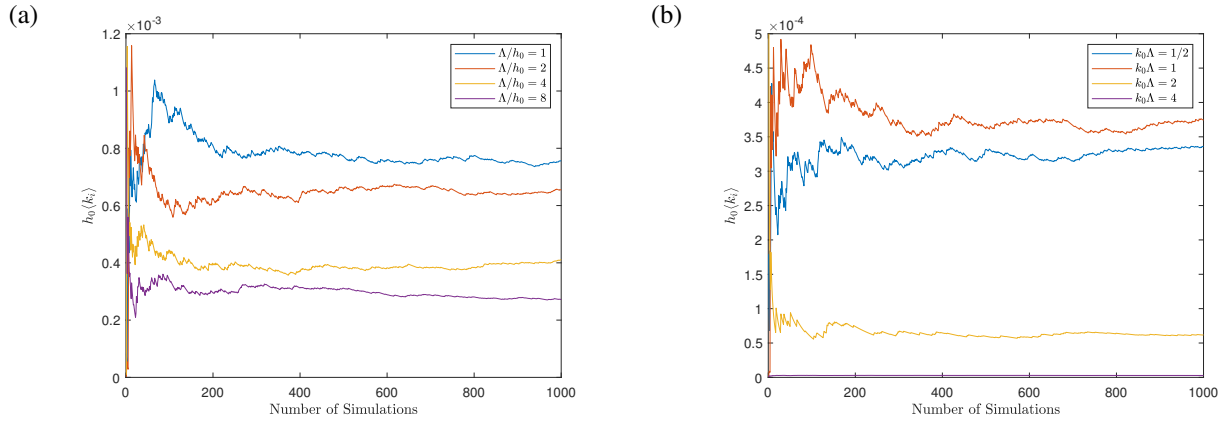


Figure 3: The variation of the dimensionless attenuation constant as  $N$ , the number of simulations, increases for random bathymetry with  $L = 400h_0$  and  $\sigma^2 = 0.02$ . In (a)  $k_0\Lambda = 1$  is fixed and  $\Lambda/h_0$  is varied; in (b)  $\Lambda/h_0 = 4$  is fixed and  $k_0\Lambda$  is varied.

changes in propagation characteristics. See, for example, the results of Mei & Black (1969) for wave propagation over a rectangular step.

We should also mention that the function describing the random beds are stored numerically at discrete points at a sufficiently high resolution that linear interpolation can be used to accurately represent  $h(x)$  and  $h'(x)$  at any intermediate points needed by the numerical integration routine.

In Figure 3 we present plots illustrating the typical convergence of the dimensionless attenuation rate,  $h_0\langle k_i \rangle$ , against  $N$ , the number of simulations. In both plots, the bed is of fixed length of  $L = 400h_0$  with vertical variations parametrised by  $\sigma^2 = 0.02$ . In one plot we fix frequency at  $k_0\Lambda = 1$  and vary  $\Lambda/h_0 = 1, 2, 4, 8$ . In the second plot we fix  $\Lambda/h_0 = 4$  and vary  $k_0\Lambda = 0.5, 1, 2, 4$ . Similar results are found when  $\sigma$  is varied with  $\Lambda/h_0$  and  $k_0\Lambda$  are held fixed. These and other tests performed suggest  $N = 500$  simulations is sufficiently large to obtain reasonable convergence to the ensemble average when balanced against computational time. We use  $N = 500$  by default occasionally increasing  $N$  when there is good reason to do so. Generally we find convergence is faster for larger  $k_0\Lambda$  and for larger  $\Lambda/h_0$  and smaller values of  $\sigma$ .

The next issue we address is the effect of bed length on convergence of the attenuation rate computed from the numerical simulation. In Fig. 4 we have fixed the bed statistics to  $\sigma^2 = 0.02$ ,  $\Lambda/h_0 = 2$  and plotted the ensemble average of dimensionless attenuation coefficient against  $k_0\Lambda$  for bed lengths increasing from  $L = 80h_0$  to  $2000h_0$ . Overlaid is the theoretical prediction for a semi-infinite bed given by (43). Thus, in Fig. 4, the numerical simulations appear to be converging to the theory as  $L \rightarrow \infty$ .

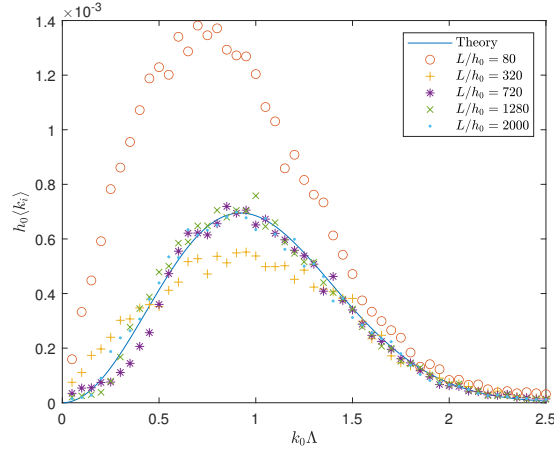


Figure 4: Non-dimensional ensemble averaged attenuation coefficient for  $N = 500$  simulations for beds of increasing length  $L$ , compared to theory. Here,  $\sigma^2 = 0.02$  and  $\Lambda = 2h_0$ .

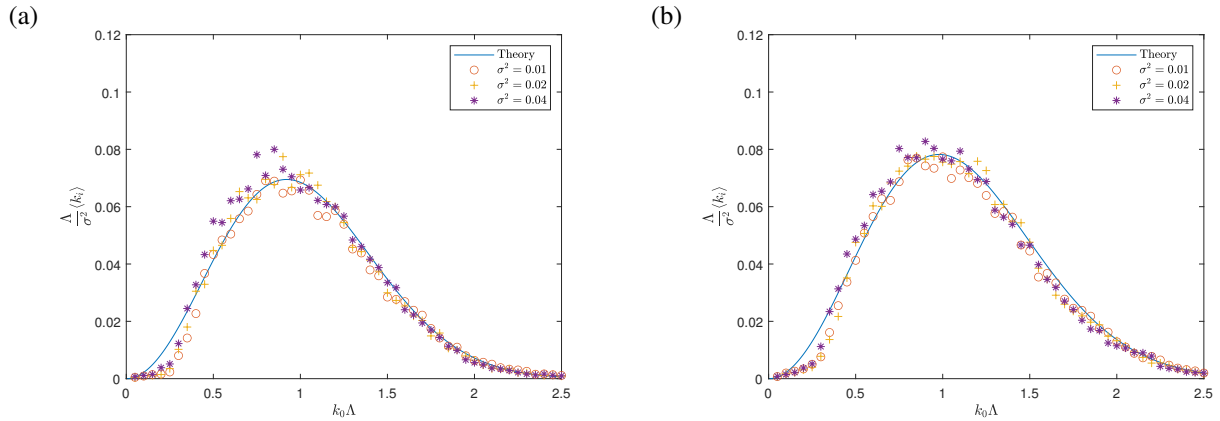


Figure 5: Scaled ensemble averaged attenuation coefficients for  $N = 500$  simulations for beds of length  $L = 10\Lambda/\sigma^2$ , compared with theory: (a)  $\Lambda/h_0 = 2$ , (b)  $\Lambda/h_0 = 4$ .

Fig. 4 indicates that the section of variable bed needs to be sufficiently long for multiple wave scattering interactions over the variable bed to accurately capture decay due to randomness. Since this is determined by calculating  $\lambda_{\pm} = e^{\mp k_i L}$  for each realisation, it is expected that  $L$  will be defined by  $k_i L = C$  for a constant  $C$  sufficiently large that variations due to randomness in eigenvalues  $\lambda_{\pm}$  of the transfer matrix  $\mathbf{P}$  remain on the real line. Extensive numerical experimentation has indicated that the rule  $k_i L = 1$ ,  $k_i$  being the theoretically-derived attenuation rate, seem to produce ensemble averages which converge across all frequencies although a small proportion of realisations still return eigenvalues from the transfer matrix indicating no attenuation. However, setting  $L$  according to the rule  $k_i L = 1$  implies increasingly long beds in both the low- and high-frequency limits. Numerical simulations become both computationally expensive and prone to rounding errors. Instead we have produced results with  $L = 10\Lambda/\sigma^2$  which has the benefit of being independent of frequency so that the same bed realisations can be used across all frequencies. In doing so are not able guarantee convergence of numerical results for  $k_0\Lambda$  such that  $k_0\Lambda e^{-k_0^2\Lambda^2/2} \lesssim 0.05\sqrt{\Lambda/\sigma^2 h_0}$ . For example, with  $\sigma^2 = 0.01$  and  $\Lambda/h_0 = 2$  this translates to  $k_0\Lambda \lesssim 0.7$ . Discrepancies between the numerical simulations and theory are noticeable at low frequencies especially for  $\sigma^2 = 0.01$  in the plots in Fig. 5. The issue of  $L$  not being sufficiently large for high frequencies does not appear to affect the results so much. Similar general comments apply later to Fig. 10, although we do notice the lack of convergence at high frequencies in the case where  $L$  takes its lowest value.

In Fig. 5 we collapse simulated data for different values of  $\sigma^2 = 0.01, 0.02, 0.04$  onto the theoretical predictions for the scaled attenuation  $\Lambda(k_i)/\sigma^2$  for two values of  $\Lambda/h_0 = 2, 4$ . The only differences in the two theoretical predictions are due to the scaling  $C_1^2$  which depends on both  $k_0\Lambda$  and  $\Lambda/h_0$ . Although there is noise in the data, we have confirmed through extensive runs of the model that the fit between the data and the theory improves as  $\sigma^2$  tends to zero. This is

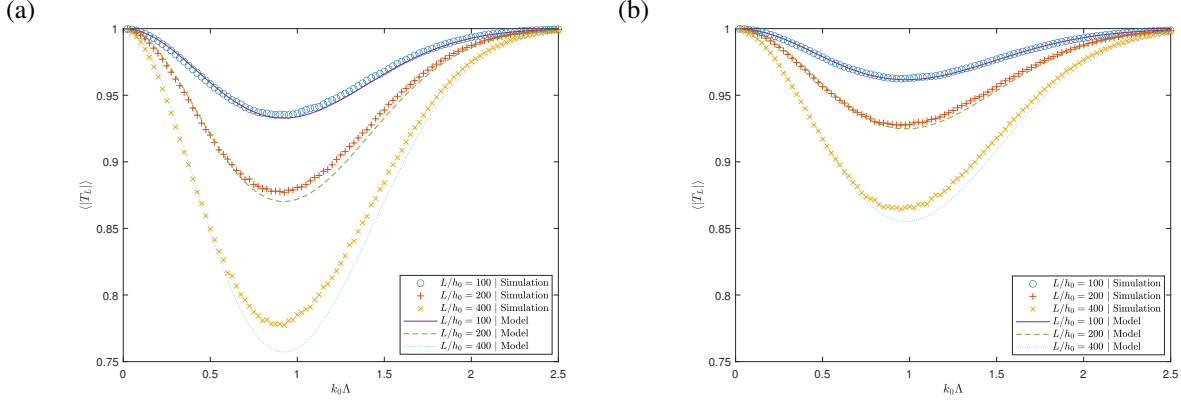


Figure 6: Variation with frequency of the ensemble average of the modulus of the transmission coefficient for  $N = 20000$  random bed simulations with statistical properties: (a)  $\sigma^2 = 0.02$ ,  $\Lambda = 2h_0$ , (b)  $\sigma^2 = 0.02$ ,  $\Lambda = 4h_0$ . Model refers to the curve fit  $\langle |T_L| \rangle = e^{-k_i L}$ .

expected since the theoretical attenuation is a leading order result from an asymptotic expansion in  $\sigma^2$ . The numerical results in Fig. 5 appear similar in character to results produced by Bennetts *et al.* (2015) in their Figure 5 where they highlighted the discrepancy between decay experienced by individual realisations and the decay predicted by their theory. These authors correctly surmise: “We deduce that the dominant source of attenuation of the effective wave elevation is wave cancellation (decoherence).” In our analysis, we identified and removed the terms which give rise to this “fictitious decay”.

In Fig. 6 we show ensemble average of the modulus of the transmission coefficient against frequency for beds with statistics  $\sigma^2 = 0.02$ ,  $\Lambda/h_0 = 2$  in one plot and  $\Lambda/h_0 = 4$  in the second, for different lengths  $L/h_0 = 100, 200, 400$ . The limit  $L \rightarrow \infty$  results in  $T_\infty = 0$ , so the convergence to this limit with increasing  $L$  is slow and the variations with  $L$  are significant. Results have been produced by averaging over 20000 simulations to produce much more accurate averages than in previous results. This is done to give a clear indication of the fit between the numerical results for  $\langle |T_L| \rangle$  for beds of finite length  $L$  and an approximate fit given by the curve  $\langle |T_L| \rangle = e^{-k_i L}$  where  $k_i$  is the attenuation rate defined by (43) for a semi-infinite bed. We offer no formal theoretical basis for this ‘model’ fit, but note it agree with exact results in both limits  $L \rightarrow 0$  and  $L \rightarrow \infty$ . Heuristically, this fit might be explained by the reflection at the junctions at  $x = 0$  and  $x = L$  between varying and constant depths being weak in comparison to the accumulated attenuation via multiple-scattering over the length of random bed.

Another model fit has been found for the ensemble average of the reflection coefficient for scattering over random beds of finite extent. These results are shown in Fig. 7 for beds of different lengths with  $N = 20000$  simulations used for averaging. The model fit  $\langle |R_L| \rangle = \sqrt{1 - e^{-\sqrt{2}k_i L}}$  to these results has no theoretical basis but appears to be remarkably accurate. We felt it useful to present this result in the event that it might have practical use or help develop new theoretical results for scattering over random beds of finite extent.

## 7 Results for randomly varying ice thickness in water of constant depth

Having presented theory and simulations in the case of variable bathymetry with no ice cover, we now consider a similar analysis of results for a fluid of constant depth  $h_0$  covered with floating broken ice submerged to a variable depth  $d(x)$ ,  $0 < x < L$ , varying randomly about  $d_0$ , with constant submergence found in  $x < 0$  and  $x > L$ . The only changes from the previous results result from different definitions for  $C_1$  and  $k_0$ . Fig. 8 shows the real and imaginary parts of the wave elevation for a single random simulation of the ice submergence  $d(x)/d_0$  illustrated in the same plot for which  $h_0 = 2d_0$  (the vertical range  $(-3, -1)$  is used to represent  $(-h_0, 0)$ .) Again, we observe the signature of partial transmission and reflection in the elevation and note the random response of the wave elevation through the variable broken ice cover.

Figure 9 illustrates how the ensemble average of the attenuation coefficient converges with  $N$ , the number of numerical simulations. Each curve is computed from a single set of realisations for particular parameters, but is typical of results across a range of parameters and convergence is identical in character to results for random bathymetry. The depth of the water in these and later results, chosen as  $h_0 = 2d_0$  may seem small for a physical setting. The primary role of the

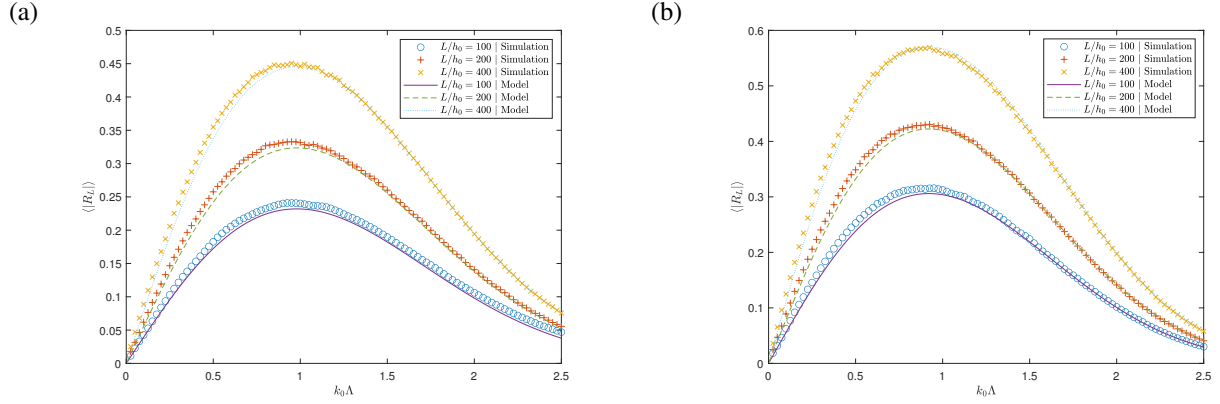


Figure 7: The ensemble average of the reflection coefficient for  $N = 20000$  simulations of random beds of varying length with statistics: (a)  $\sigma^2 = 0.02, \Lambda = 2h_0$ , (b)  $\sigma^2 = 0.02, \Lambda = 4h_0$ . The model fit are curves given by  $\langle |R_L| \rangle = \sqrt{1 - e^{-\sqrt{2}k_t L}}$ .

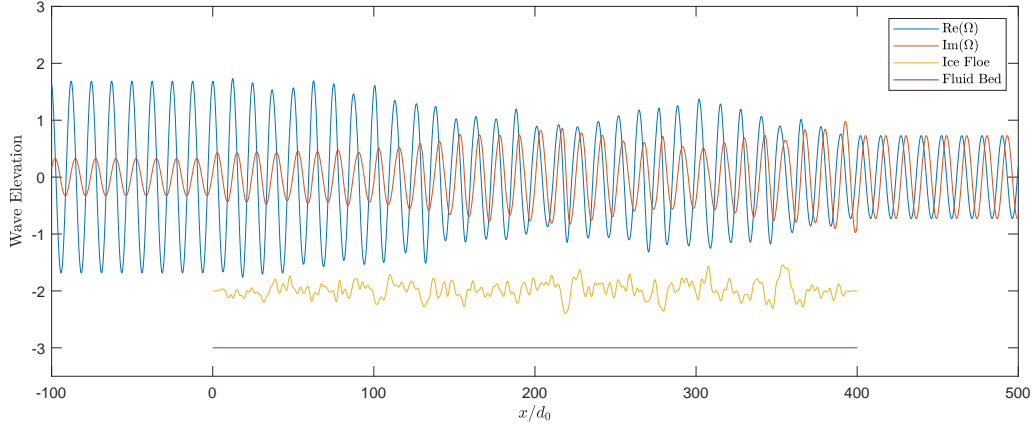


Figure 8: An example of the wave elevation (real and imaginary parts of  $\Omega(x)$ ) and an overlay of the random function representing ice submergence across  $0 < x < L$ . Here,  $\sigma^2 = 0.02, \Lambda = 2d_0$  and  $L = 400d_0$  and the fluid depth is  $h_0 = 2d_0$ .

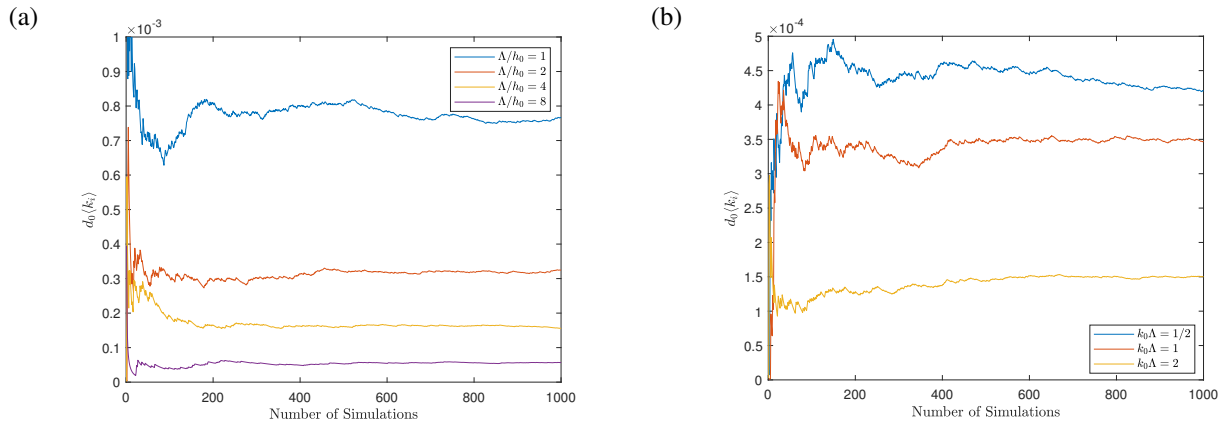


Figure 9: The variation of the non-dimensional attenuation coefficient with increasing  $N$ , the number of simulations in the case of randomly varying ice thickness with  $\sigma^2 = 0.02, L = 400d_0$  and  $h_0 = 2d_0$ . In (a)  $k_0 \Lambda = 1$  is fixed and  $\Lambda/h_0$  is varied; in (b)  $\Lambda/h_0 = 4$  is fixed and  $k_0 \Lambda$  is varied.

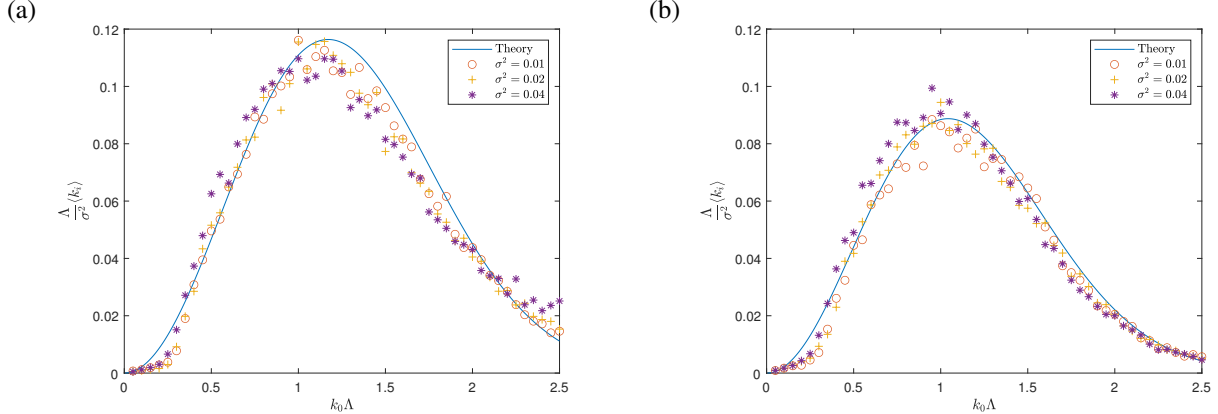


Figure 10: Scaled attenuation coefficient averaged over  $N = 500$  simulations of random ice over distance defined by  $L = 10\Lambda/\sigma^2$  compared with theoretical predictions. Here,  $h_0 = 2d_0$ ,  $\sigma$  is varied (see legend) and (a)  $\Lambda = 2d_0$ , (b)  $\Lambda = 4d_0$ .

depth is in setting the wavenumber  $k_0$  in terms of the frequency,  $K$ . The choice  $h_0 = 2d_0$  allows us to extend the range of values of  $K$  over which the results can be presented without violating the assumptions of shallowness.

Figure 10 show results which are analogous to those obtained in Figure 5, comparing the attenuation coefficient calculated by ensemble averaging numerically-determined decay over 500 realisations of a long finite variable ice cover against theoretical results. The vertical axis is scaled so that results for different values of  $\sigma$  can be collapsed onto a single theoretical curve. The results for random ice cover differ from those for random bathymetry only in the definition of  $k_0$  and  $C_1$  for ice.

In the final part of the results, we consider the application of the theoretical model for attenuation through continuous broken with field measurements from a number of different studies. This exercise is intended to demonstrate that randomly-varying ice thickness is plausible physical mechanism for attenuation of waves observed through regions of broken ice. We are not suggesting that the model in this paper is directly applicable to any of the different physical settings. In particular, our model is two-dimensional and many simplifying assumptions have been made including that the combined water/ice depth is small compared to the wavelength. In addition to depth, the complexity of ice composition, which exists in different forms such as pancake, grease or frazil ice and the percentage of open water coverage of the ice are features which our model neglects.

On the other hand, there has been a longstanding campaign (see, for example, Squire *et al.* (1995)) to develop plausible models which capture the power law relationship between wave frequency and attenuation coefficients. Analysis of historical field measurements by Meylan *et al.* (2018) suggest attenuation scales like  $\omega^n$  for  $n$  between 2 and 4 (see Fig. 11(b)). Our model predicts attenuation scales like  $k_0^2$  (for long waves) and since  $k_0$  scales like  $\omega$  under shallow water assumptions, it follows that attenuation scales like  $\omega^2$ , in line with observations. Furthermore, it is perfectly possible for an analogous deep-water theory for attenuation to be derived, following methods Bennetts *et al.* (2015) but modified suitably to remove fictitious decay and this would inevitably predict attenuation that scales like  $k_0^2$  (for long waves). Since  $k_0$  scales like  $\omega^2$  for deep water the resulting in attenuation scaling in this case would scale like  $\omega^4$ . Thus, the low frequency model we have developed is compatible with the range of results seen in field measurements.

One of the principle features described in Squire *et al.* (1995), which include field measurements of Wadhams *et al.* (1988) and Liu *et al.* (1992), is that of “roll-over”. This is the observation that the attenuation rates peak and start to drop as the frequency increases beyond a critical value. High-frequency roll-over effects have since been disputed, most notably in Rogers *et al.* (2016) and Thomson *et al.* (2021), although roll-over is a highlighted feature of the recent data of Doble *et al.* (2015) (see their Figure 2). Our theoretical results do predict a peak in attenuation and supports the evidence for a high-frequency roll-over effect. However, we need also to be mindful of the limitations of our theory which is that it is formally limited to low frequencies and high-frequency effects require a different theoretical approach.

In Figs. 11 and 12 we have gone further and shown how other features of the theoretical attenuation coefficient derived in this paper exhibit a qualitative fit over four different sets of published field data (references are displayed under each figure panel). In Figs. 11, the shallow water dispersion relation (7) is used to determine the frequency (or period) from the wavelength (or wavenumber). Our assertion is that scattering by randomness in the ice cover primarily relates to

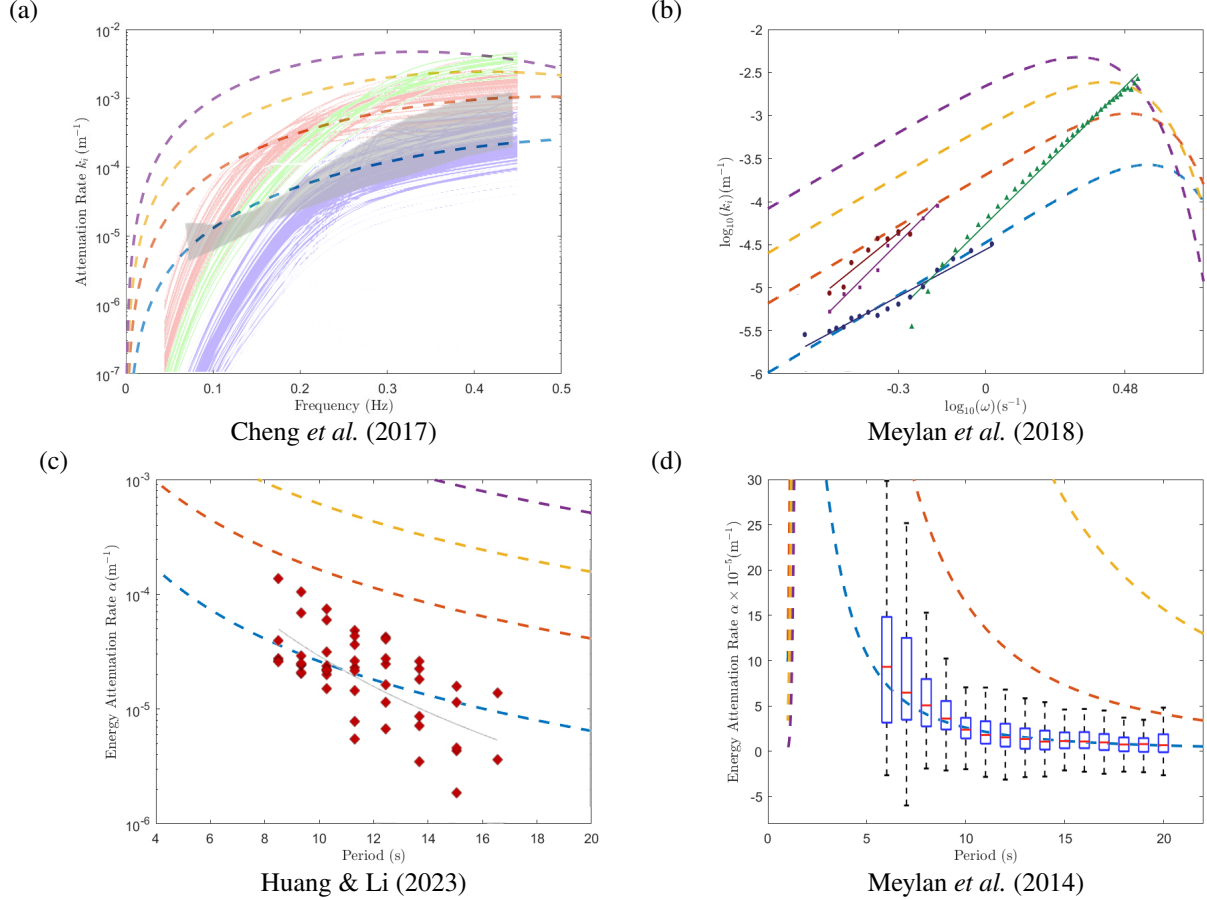


Figure 11: Attenuation rates ( $\alpha = 2k_i$ ) based on our theory for varying ice depth superimposed onto field data taken from sources quoted in each sub-figure. The background ice submergence takes values  $d_0 = 10\text{cm}$  (blue),  $20\text{cm}$  (red),  $30\text{cm}$  (yellow) and  $40\text{cm}$  (magenta) and all other parameters are fixed. The shallow water dispersion relation is used to determine frequency/period.

the wavelength rather than the frequency (or depth). Thus, in Figs. 12 we have used the deep-water dispersion relation  $\omega = \sqrt{gk_0}$  to determine the frequency (or period) even though the attenuation is predicted by a shallow-water model. In each set of results we have superimposed theoretical curves (dashed) onto plots published in each cited piece of work.

We fix  $h_0 = 1$  in all plots. This may be regarded as a fitting parameter rather than representative of the actual depth; altering  $h_0$  changes the shape but not the character of the curves and  $h_0 = 1$  happens to provide a good fit. According to data sources listed in the bibliography, typical ice thickness varies over the range of  $5\text{cm}$  to  $50\text{cm}$  and we consider varying the background depth of submergence from  $d_0 = 10\text{cm}$  to  $d_0 = 40\text{cm}$ . The statistical parameters associated with the ice were chosen by assuming roll-over exists and estimating from the Figure of Cheng *et al.* (2017) – who reproduces curves in Rogers *et al.* (2016) (both shown in our Fig. 11) – that a peak attenuation  $k_i \approx 1 \times 10^{-3}$  occurs at the frequency  $0.45\text{Hz}$  for the ice submergence of  $d_0 = 25\text{cm}$  (the mean ice thickness measured by Wadhams *et al.* (2004) was  $24\text{cm}$ ). This allows us to deduce  $\Lambda$  from our theoretical result (close to  $k_0\Lambda = 1$ ) after deducing  $k_0$  from frequency via the appropriate dispersion relation. Finally, the value of  $\sigma$  is deduced by matching the height of the peak to the data. For the shallow water dispersion relation, we find  $\Lambda \approx 0.94\text{m}$  and  $\sigma^2 \approx 0.067$  and these are used to produce the dashed line curves in Figs. 11 for  $d_0 = 10\text{cm}$  to  $40\text{cm}$ . When the deep-water dispersion relation is used, we find  $\Lambda \approx 1.45\text{m}$  and  $\sigma^2 \approx 0.13$  and these values are used to produce the dashed line curves Figs. 12. Although we are fitting parameters to the data, it is useful to see that the same fixed parameters follow the broad trends seen across the range of data available and that the spread of data can be attributed to different ice thickness (also see data in support of this published in Rogers *et al.* (2021)). In particular, Figs. 12 relating to the deep-water dispersion frequency provides an excellent fit to the data. We have chosen not to describe the precise nature of the data presented in the figures which can be found in each of the references; the figures are intended only to provide a visual guide.

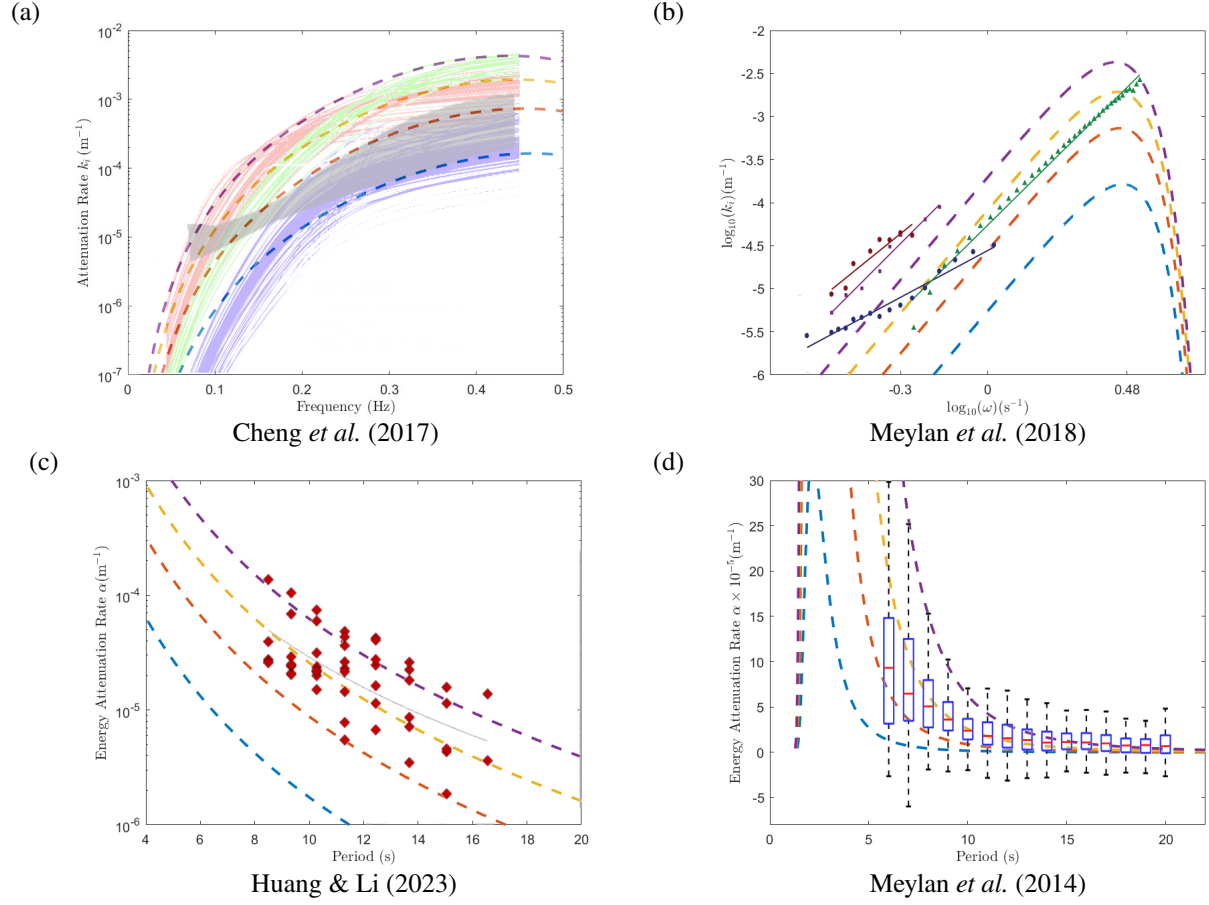


Figure 12: Attenuation rates ( $\alpha = 2k_i$ ) based on our theory for varying ice depth superimposed onto field data taken from sources quoted in each sub-figure. The background ice submergence takes values  $d_0 = 10\text{cm}$  (blue),  $20\text{cm}$  (red),  $30\text{cm}$  (yellow) and  $40\text{cm}$  (magenta) and all other parameters are fixed. The deep water dispersion relation is used to determine frequency/period.

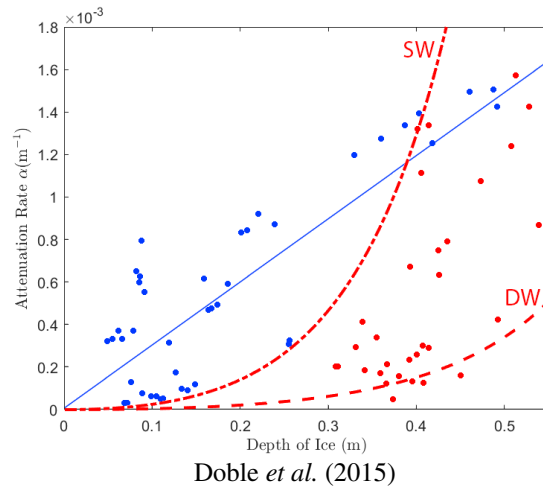


Figure 13: Attenuation rate of energy,  $\alpha = 2k_i$ , against ice thickness. Results of Doble et al. (2015) (dots: data and blue curve: linear fit to blue dots) and our theory for a shallow water dispersion relation (SW: chained red curve) and deep water dispersion relation (DW: dashed red curve) using values of  $h_0 = 1\text{m}$ , period 8s,  $\Lambda$  and  $\sigma$  determined from Figs. 11 and 12 respectively.

In Fig. 13 we compare the variation of  $\alpha = 2k_i$  (the energy attenuation rate) with  $d_0$  against the field data presented in Figure 2 of the work of Doble *et al.* (2015) is represented by the dots and using the same colour scheme as in their Figure. Also superimposed is the blue line of Doble *et al.* (2015) which they added to indicate a linear fit through data coloured blue which was attributed to measurements taken while ice was being placed under a compressive state. In contrast the red dots were attributed to ice in a state of expansion and, in their paper, Doble *et al.* (2015) explain: “*The expansion case is less defined, and on a significantly different gradient. We attribute this deviation to very heterogeneous ice thickness during expansion, when the rafted pancake ice would diverge in a clumpy manner.*” Curves from our theory have been superimposed (red lines) onto the data of Doble *et al.* (2015). Since the theory states  $k_i \propto C_1^2$  and  $C_1^2 \propto d_0^2/(h_0 - d_0)^2$  and we are using  $h_0 = 1\text{m}$ , as before, our model predicts an underlying quadratic behaviour to the attenuation with increasing ice thickness. As can be seen, this happens to agree well with the data (red dots) from the non-compressive/rafting phase of the ice dynamics. In the plots, we use the same period of 8s as Doble *et al.* (2015) and have re-used the same values of  $\Lambda$  and  $\sigma$  stated earlier from the fitting to the data of Cheng *et al.* (2017) in Figs. 11 and 12. Additional extensive modern sets of data described in Kohout *et al.* (2020) have been used in the papers of Rogers *et al.* (2021) and Montiel *et al.* (2022) and can be used to show similar model agreement<sup>1</sup>, although there is greater focus on effects such as wave height and ice concentration which are not captured in the current model.

## 8 Conclusions

The paper has considered a basic model for the propagation of long waves through water of variable shallow depth with a surface covered by fragmented broken ice. Simple expressions have been derived for the attenuation of waves over randomly-varying bathymetry and through ice of randomly-varying thickness. In the analytic derivation of the expression for attenuation based on randomness occupying a semi-infinite domain, we have identified and removed terms responsible for incoherent phase cancellations in the ensemble averaging process which contribute to fictitious decay not experienced by individual realisations of wave propagation through randomness. The theory has been shown to agree with numerical simulations in which averaging was performed over individual wave realisations across randomness of finite extent. In the simulations, for which our shallow-water models require numerical solutions to simple two-dimensional ODEs, attenuation was measured accurately by computing eigenvalues of the resulting transfer matrix. These encode propagation but exclude multiple scattering effects relating to transitions at the ends of the scattering region from variable to constant parameter values.

In addition to resolving the discrepancy between theory and numerical simulations for random bathymetry highlighted by Bennetts *et al.* (2015), we have also shown that there is a peak in attenuation which relate closely to a Bragg resonant effect, the significant lengthscale of the bed being its statistical correlation length. Beyond this peak, attenuation decreases exponentially as a function of the square of the wavenumber. This decay, predicted by the shallow-water model, therefore appears not to be a finite-depth effect as proposed in some previous studies (e.g. Devillard *et al.* (1988), Mei *et al.* (2005)).

The shallow-water formulation has been extended to include the effect of broken ice using the method of Porter (2019). This second-order extension of the classical shallow-water model includes vertical acceleration which is needed for the ice thickness to enter the dynamics. After confirming agreement between theory and numerical simulations we have made some comparisons between the theoretical predictions based upon our basic model and a number of sets of available field data. Depending upon how the wavelength through ice of random thickness is related to frequency (i.e. using the shallow water or equivalent deep water dispersion relation) the attenuation is shown to scale with angular frequency like  $\omega^2$  or  $\omega^4$  for long waves. This is in line with field observations, whilst the peak in the attenuation for higher frequencies can explain the “roll-over effect” seen in many data sets. We have also used our model to show that there is overlap between theory and field data for the dependence of attenuation on ice thickness, with our result suggesting attenuation scales as the square of the thickness.

Whilst our model has been used to demonstrate agreement with field data for attenuation through ice, we are mindful that the model is highly simplified, in contrast to the complex physical nature of floating ice and its interaction with the ocean. Although parameters including the water depth and the statistical properties of the ice have been determined by fitting to (one set of) data, we have demonstrated that the same parameter sets are capable of reproducing acceptable fits to four other sets of data. This gives us good reason to believe that random variations in ice thickness could be a plausible mechanism for the attenuation of waves through broken sea ice. We plan a range of extensions to the current work to include more complex effects which include: (i) finite water depth; (ii) variable ice cover concentration; (iii) discrete ice floe models; (iv) weak non-linearity and (v) three-dimensional scattering.

**[Funding]** L.D. is grateful for the support of an EPSRC (UK) studentship.

<sup>1</sup>The online graphical abstract shows a comparison of our model with data published in Rogers *et al.* (2021).

[**Declaration of interests**] The authors report no conflict of interest.

[**Data availability statement**] The data used to produce the figures in this study are openly available at <https://figshare.com/175050>

[**Author ORCIDs**]

① L. Dafydd, <https://orcid.org/0000-0003-1009-0946>

① R. Porter, <https://orcid.org/0000-0003-2669-0188>

## Appendix: Derivation of the long wave model

The model will be developed in a two-dimensional Cartesian framework  $(x, z)$  with  $z$  directed vertically upwards. Fluid of density  $\rho$  is bounded below by a rigid bed located at  $z = -h(x)$  and above by freely-floating fragmented ice of thickness  $d(x)\rho/\rho_i$  where  $\rho_i$  is the density of ice. The moving fluid/ice interface is described by  $z = -d(x) + \zeta(x, t)$  where  $\zeta(x, t)$  represent the wave elevation and  $t$  is time. Thus the rest position of an unloaded fluid surface would be  $z = 0$ .

We assume that the depth is small compared to the wavelength and that gradients of  $h(x)$  and  $d(x)$  are equally small. The ice is assumed broken into individual floes whose horizontal extent is small compared to the wavelength. The floes are constrained to move vertically. The length of individual floes does not enter our model since we assume a continuum model from the outset (the description of the ice submergence as  $d(x)$  already indicates this) which avoids engaging in a formal derivation based on multiple horizontal scales.

The fluid is assumed to be both inviscid and incompressible and its motion is represented by the velocity field  $(u(x, z, t), w(x, z, t))$ ,  $u$  and  $w$  being the horizontal and vertical components of the flow respectively.

Within the fluid, conservation of mass requires

$$u_x + w_z = 0 \quad (\text{A.1})$$

is satisfied. Conservation of momentum gives

$$\rho u_t + \rho(uu_x + wu_z) = -p_x, \quad \text{and} \quad \rho w_t + \rho(uw_x + ww_z) = -p_z \quad (\text{A.2})$$

where  $p(x, z, t)$  is the *dynamic* pressure in the fluid in excess of background hydrostatic pressure  $-\rho g z$  where  $g$  is acceleration due to gravity and the background atmospheric pressure above the ice is assumed without loss of generality to be zero. On the rigid bed, the no flow condition is represented by

$$w + h'(x)u = 0, \quad \text{on } z = -h(x), \quad (\text{A.3})$$

and on the moving fluid/ice interface we have the kinematic and dynamic conditions

$$\zeta_t = w + d'(x)u, \quad \text{on } z = -d(x) + \zeta(x, t), \quad (\text{A.4})$$

and

$$\rho d(x)\zeta_{tt} = p(x, -d(x) + \zeta(x, t), t) - \rho g \zeta(x, t). \quad (\text{A.5})$$

We rescale physical variables using

$$x = Lx^*, \quad z = Hz^*, \quad h = Hh^*, \quad d = Hd^* \quad \text{and} \quad \zeta = A\zeta^*, \quad (\text{A.6})$$

where  $L$  represents a characteristic horizontal lengthscale (a different definition from the one used in the main part of the text for the length of the bed) associated with the wavelength and/or the variable bed/ice cover,  $H$  is a characteristic fluid depth and  $A$  a characteristic wave elevation. We also define

$$\epsilon = \frac{H}{L}, \quad \delta = \frac{A}{H} \quad (\text{A.7})$$

which represents shallowness and wave steepness respectively. We suppose that both  $\epsilon$  and  $\delta$  are small and assume that  $\delta = o(\epsilon^2)$  to ensure we operate within a linearised setting.

Based on the shallow water dispersion relation, we select a timescale  $T = L/\sqrt{gH}$  so that  $t = Lt^*/\sqrt{gH}$  and set

$$u = \frac{A}{H}\sqrt{gH}u^* \quad \text{and} \quad w = \frac{A}{L}\sqrt{gH}w^* \quad (\text{A.8})$$

whilst  $p = \rho g A p^*$ . Under this change of variables the governing equations become (after dropping asterisks)

$$u_x + w_z = 0 \quad (\text{A.9})$$

with

$$u_t + \delta(uu_x + wu_z) = -p_x \quad (\text{A.10})$$

and

$$\epsilon^2 w_t + \delta \epsilon^2 (uw_x + ww_z) = -p_z. \quad (\text{A.11})$$

Our boundary condition at the fluid bed reads

$$w + h'(x)u = 0 \quad \text{on } z = -h(x) \quad (\text{A.12})$$

with our boundary conditions on the ice becoming

$$\zeta_t = w + d'(x)u, \quad \text{on } z = -d(x) + \delta \zeta(x, t) \quad (\text{A.13})$$

and

$$\epsilon^2 d(x)\zeta_{tt} = p(x, -d(x) + \delta \zeta(x, t), t) - \zeta. \quad (\text{A.14})$$

Noting that  $\delta = o(\epsilon^2)$  has been assumed we expand variables up to  $O(\epsilon^2)$ , so that

$$\zeta(x, t) = \zeta^{(0)}(x, t) + \epsilon^2 \zeta^{(1)}(x, t) + \dots \quad (\text{A.15})$$

and

$$\{p, u, w\}(x, z, t) = \{p^{(0)}, u^{(0)}, w^{(0)}\}(x, z, t) + \epsilon^2 \{p^{(1)}, u^{(1)}, w^{(1)}\}(x, z, t) + \dots \quad (\text{A.16})$$

Only in the case that  $h(x)$  and/or  $d(x)$  contain discontinuities would we need to include terms of  $O(\epsilon)$  (see, Mei *et al.* (2005)) since these would arise from an asymptotic matching process across the discontinuity. It is consistent with this expansion that we neglect contributions from terms multiplying  $\delta$  in (A.9)-(A.14). We continue by solving for the leading order variables. From (A.11),  $p_z^{(0)} = 0$  and from (A.14),  $p^{(0)}(x, -d(x), t) = \zeta^{(0)}(x, t)$  implies

$$p^{(0)}(x, z, t) = \zeta^{(0)}(x, t) \quad (\text{A.17})$$

and then from (A.10) we have

$$u_t^{(0)}(x, z, t) = -\zeta_x^{(0)}(x, t) \quad (\text{A.18})$$

and so  $u^{(0)}$  is a function of  $x$  and  $t$  only. Integrating (A.9) at leading order from  $z = -h(x)$  to  $z = -d(x)$  and using (A.12) and (A.13) gives

$$q_x^{(0)}(x, t) = \left( (h(x) - d(x))u^{(0)}(x, t) \right)_x = -\zeta_t^{(0)}(x, t) \quad (\text{A.19})$$

where we have defined the depth-integrated horizontal fluid flux  $q(x, t) = q^{(0)}(x, t) + \epsilon^2 q^{(1)}(x, t) + \dots$  with

$$q^{(0,1)}(x, t) = \int_{-h(x)}^{-d(x)} u^{(0,1)}(x, z, t) dz. \quad (\text{A.20})$$

Eliminating between (A.18) and (A.19) gives either

$$\zeta_{tt}^{(0)} = \left( (h(x) - d(x))\zeta_x^{(0)} \right)_x, \quad \text{or} \quad q_{tt}^{(0)} = (h(x) - d(x))q_{xx}^{(0)} \quad (\text{A.21})$$

as the leading order governing equation, expressed in dimensionless variables. That is, the effect of fragmented ice cover at leading order is equivalent to an uncovered fluid having a reduced depth,  $h(x) - d(x)$ .

Now we work at the next order,  $O(\epsilon^2)$ . Integrating (A.9) at order  $O(\epsilon^2)$  from  $z = -h(x)$  to  $z = -d(x)$  and using (A.12) and (A.13) at  $O(\epsilon^2)$  gives

$$q_x^{(1)}(x, t) = \frac{\partial}{\partial x} \int_{-h(x)}^{-d(x)} u^{(1)}(x, z, t) dx = -\zeta_t^{(1)}(x, t). \quad (\text{A.22})$$

The next step is to determine the leading order vertical velocity integrating (A.9) again, but now from  $z$  to  $-d(x)$  to give

$$w^{(0)}(x, z, t) = \zeta_t^{(0)}(x, t) - \left( (z + d(x))u^{(0)}(x, t) \right)_x \quad (\text{A.23})$$

which is linear in  $z$ . From (A.11) at  $O(\epsilon^2)$  we infer that

$$p_z^{(1)}(x, z, t) = -\zeta_{tt}^{(0)} + \left( (z + d(x))u_t^{(0)} \right)_x \quad (\text{A.24})$$

which can be integrated using the condition (A.14) at  $O(\epsilon^2)$  to give

$$p^{(1)}(x, z, t) = \zeta^{(1)} - z\zeta_{tt}^{(0)} + \frac{1}{2} \left( (z + d(x))^2 u_t^{(0)} \right)_x. \quad (\text{A.25})$$

Using in (A.10) at  $O(\epsilon^2)$  gives

$$u_t^{(1)}(x, z, t) = -p_x^{(1)} = z\zeta_{tt}^{(0)} - \zeta_x^{(1)} - \frac{1}{2} \left( (z + d(x))^2 u_t^{(0)} \right)_{xx}. \quad (\text{A.26})$$

We find, after extensive algebra, which makes repeated use of the relation  $q_t^{(0)} = (h - d)u_t^{(0)}$ , that

$$\begin{aligned} q_t^{(1)}(x, t) = \int_{-h(x)}^{-d(x)} u_t^{(1)} dz = \frac{1}{2}(d^2 - h^2)\zeta_{tt}^{(0)} - (h - d)\zeta_x^{(1)} + \frac{1}{2}(h - d)d''q_t^{(0)} \\ - \frac{1}{6} \left\{ (h - d)'q_{xxt}^{(0)} - 2(h - d)(h' - d')q_{xt}^{(0)} - (h'' - d'')(h - d)q_t^{(0)} + 2(h' - d')^2q_t^{(0)} \right\} \\ - d'^2q_t^{(0)} + d' \left\{ (h - d)q_{xt}^{(0)} - (h' - d')q_t^{(0)} \right\}. \end{aligned} \quad (\text{A.27})$$

Further simplification and use of the relation  $q_x^{(0)} = -\zeta_t^{(0)}$  results in

$$\begin{aligned} q_t^{(1)} = -(h - d) \left( \zeta_x^{(1)} + \frac{1}{3} \left( (h + 2d)\zeta_{tt}^{(0)} \right)_x \right) \\ + q_t^{(0)} \left( \frac{1}{6}(h - d)(h + 2d)'' - \frac{1}{3}(h - d)'(h + 2d)' - d'^2 \right). \end{aligned} \quad (\text{A.28})$$

We can now recombine leading order and  $O(\epsilon^2)$  terms as we redimensionalise variables, a process which leads to the coupled equations

$$\zeta_t = -q_x \quad (\text{A.29})$$

and

$$\left( 1 + d'^2 + \frac{1}{3}(h - d)'(h + 2d)' - \frac{1}{6}(h - d)(h + 2d)'' \right) q_t = -(h - d) \left( g\zeta + \frac{(h + 2d)}{3}\zeta_{tt} \right)_x \quad (\text{A.30})$$

expressed in terms of the original physical variables  $q$  and  $\zeta$  and which are accurate to  $O(\epsilon^2)$ . Eliminating  $q$  in favour of  $\zeta$  gives us the governing equation

$$\zeta_{tt} = \frac{\partial}{\partial x} \left( \hat{d}(x) \frac{\partial}{\partial x} \left( g\zeta + \frac{(h + 2d)}{3}\zeta_{tt} \right) \right) \quad (\text{A.31})$$

where

$$\hat{d}(x) = \frac{(h - d)}{1 + d'^2 - \frac{1}{6}(h - d)(h + 2d)'' + \frac{1}{3}(h - d)'(h + 2d)'}. \quad (\text{A.32})$$

Note that when  $d(x) \equiv 0$  we recover equation (2.13) from Porter (2019). We see that the expansion to  $O(\epsilon^2)$  in the small parameter  $\epsilon = H/L$  has captured the contribution from the inertia of the ice in (A.31) whilst there are non-trivial modifications to the wave speed through the geometrical factors associated with varying  $d(x)$  and  $h(x)$  in (A.32). Specifically, is worth noting that  $(h + 2d)/3 = (h - d)/3 + d$  and  $h - d$  is the vertical extent of the fluid. Thus, the isolated contribution  $d\zeta_{tt}$  is associated with ice inertia and the remaining  $\frac{1}{3}(h - d)\zeta_{tt}$  is a contribution from vertical acceleration of the fluid through depth-averaging, in common with Porter (2019).

Eliminating  $\zeta$  in favour of  $q$  between (A.29) and (A.30) gives

$$q_{tt} = \hat{d}(x) \left( gq_x + \frac{(h + 2d)}{3}q_{ttx} \right)_x \quad (\text{A.33})$$

and this provides the starting point for a series of transformations of the dependent variable which follow Porter (2019). We factorise a time-harmonic variation with

$$q(x, t) = \Re \left\{ \frac{\varphi(x)}{\sqrt{1 - \frac{1}{3}K(h + 2d)}} e^{-i\omega t} \right\} \quad (\text{A.34})$$

and the square-root factor in the denominator simultaneously transforms the resulting ODE into canonical form. Thus, after some algebra we find

$$\varphi''(x) + \left( \frac{\hat{K}}{h - d} \left( 1 + \frac{1}{3}v_1(h, d)h'(x)^2 + \frac{1}{3}v_2(h, d)(d'(x)^2 + h'(x)d'(x)) \right) \right) \varphi(x) = 0 \quad (\text{A.35})$$

where

$$\hat{K} = \frac{K}{1 - \frac{1}{3}K(h + 2d)}, \quad (\text{A.36})$$

$$v_1(h, d) = 1 + \frac{1}{12}\hat{K}(h(x) - d(x)) \quad \text{and} \quad v_2(h, d) = 1 + \frac{1}{3}\hat{K}(h(x) - d(x)). \quad (\text{A.37})$$

A final change of variables is made, by letting  $\Omega(x) = \varphi'(x)$  and it follows that (A.35) is transformed into

$$(\hat{d}(x)\Omega')' + K\Omega = 0 \quad (\text{A.38})$$

where

$$\hat{d}(x) = \frac{(h - d)(1 - \frac{1}{3}K(h + 2d))}{1 + \frac{1}{3}v_1(h, d)h'(x)^2 + \frac{1}{3}v_2(h, d)(d'(x)^2 + h'(x)d'(x))}. \quad (\text{A.39})$$

This final series of transformations have brought about two useful features. The first is that (A.38) is expressed in a form aligned with the familiar linearised first order shallow water equation. The second is that the function  $\Omega(x)$  and its derivative  $\Omega'(x)$  are continuous even if  $h'(x)$  and/or  $d'(x)$  are discontinuous. The free surface be reconstructed from  $\Omega(x)$  by following the effect of each transformation and turns out to be represented by

$$\eta = \frac{(-i/\omega)}{\sqrt{1 - \frac{1}{3}K(h + 2d)}} \left( \Omega(x) - \frac{\frac{1}{6}(h - d)(h + 2d)'}{1 + \frac{1}{3}v_1(h, d)h'(x)^2 + \frac{1}{3}v_2(h, d)(d'(x)^2 + h'(x)d'(x))} \Omega'(x) \right) \quad (\text{A.40})$$

where  $\zeta(x, t) = \Re\{\eta(x)e^{-i\omega t}\}$ .

Since we anticipate  $Kh \ll 1$ , we can make approximations  $v_1(h, d) \approx 1$  and  $v_2(h, d) \approx 1$ , noting  $0 < h - d \leq h$  and so

$$\frac{1}{3}v_1(h, d)h'(x)^2 + \frac{1}{3}v_2(h, d)(d'(x)^2 + h'(x)d'(x)) \approx \frac{1}{3}(h'(x)^2 + h'(x)d'(x) + d'(x)^2). \quad (\text{A.41})$$

We note that if we let  $d(x) = 0$  in (A.39), (A.40) and (A.41) we recover expressions derived in Porter (2019).

## References

- ANDERSON, P.W. 1958 Absence of diffusion in certain random lattices. *Phys. Rev.* **109** (5), 1492–1505.
- BELZONS, M., GUAZZELLI, E. & PARODI, O. 1988 Gravity waves on a rough bottom: Experimental evidence of one-dimensional localization. *J. Fluid Mech.* **186**, 539–558.
- BENNETTS, L.G., PETER, M.A. & CHUNG, H. 2015 Absence of localisation in ocean wave interactions with a rough seabed in intermediate water depth. *Q. J. Mech. Appl. Math.* **68** (1), 97–113.
- CHENG, S., ROGERS, W.E., THOMSON, J., SMITH, M., DOBLE, M.J., WADHAMS, P., KOHOUT, A.L., LUND, B., PERSSON, O.P.G., III, C.O. COLLINS, ACKLEY, S.F., MONTIEL, F. & SHEN, H.H. 2017 Calibrating a viscoelastic sea ice model for wave propagation in the arctic fall marginal ice zone. *J. Geophys. Res.: Oceans* **122** (11), 8770–8793.
- DEVILLARD, P., DUNLOP, F. & SOUILLARD, B. 1988 Localization of gravity waves on a channel with a random bottom. *J. Fluid Mech.* **186**, 521–538.
- DOBLE, M.J., CAROLIS, G. DE, MEYLAN, M.H., BIDLOT, J.-R. & WADHAMS, P. 2015 Relating wave attenuation to pancake ice thickness, using field measurements and model results. *Geophys. Res. Lett.* **42** (11), 4473–4481.
- GRATALOUP, G.L. & MEI, C.C. 2003 Localization of harmonics generated in nonlinear shallow water waves. *Phys. Rev. E* **68** (2), 026314.
- HUANG, B. & LI, X. 2023 Wave attenuation by sea ice in the arctic marginal ice zone observed by spaceborne SAR .
- KAWAHARA, M., YOSHIMURA, N., NAKAGAWA, K. & OHSAKA, H. 1976 Steady and unsteady finite element analysis of incompressible viscous fluid. *Int. J. Numerical Methods Eng.* **10** (2), 437–456.
- KOHOUT, A.L., SMITH, M., ROACH, L.A., WILLIAMS, G., MONTIEL, F. & WILLIAMS, M.J.M. 2020 Observations of exponential wave attenuation in antarctic sea ice during the pipers campaign. *Annals of Glaciology* **61** (82), 196–209.
- LIU, A.K., VACHON, P.W., PENG, C.Y. & BHOGAL, A.S. 1992 Wave attenuation in the marginal ice zone during limex. *Atmosphere-Ocean* **30** (2), 192–206.
- MEI, C.C. & BLACK, J. 1969 Scattering of surface waves by rectangular obstacles in waters of finite depth. *J. Fluid Mech.* **38**, 499–511.

- MEI, C.C. & LI, Y. 2004 Evolution of solitons over a randomly rough seabed. *Phys. Rev. E* **70** (1), 016302.
- MEI, C.C., STIASSNIE, M. & YUE, D.K.P. 2005 *Theory and applications of Ocean Surface Waves*. World Scientific.
- MEYLAN, M.H., BENNETTS, L.G. & KOHOUT, A.L. 2014 In situ measurements and analysis of ocean waves in the antarctic marginal ice zone. *Geophys. Res. Lett.* **41** (14), 5046–5051.
- MEYLAN, M.H., BENNETTS, L.G., MOSIG, J.E.M., ROGERS, W.E., DOBLE, M.J. & PETER, M.A. 2018 Dispersion relations, power laws, and energy loss for waves in the marginal ice zone. *J. Geophys. Res.: Oceans* **123** (5), 3322–3335.
- MONTIEL, F., KOHOUT, A.L. & ROACH, L.A. 2022 Physical drivers of ocean wave attenuation in the marginal ice zone. *J. Phys. Oceanography* **52** (5), 889–906.
- NACHBIN, A. 1995 The localization length of randomly scattered water waves. *J. Fluid Mech.* **296**, 353–372.
- NACHBIN, A. & PAPANICOLAOU, G.C. 1992a Boundary element methods for long-time water wave propagation over rapidly varying bottom topography. *Int. J. Numerical Methods in Fluids* **14**, 1347–1365.
- NACHBIN, A. & PAPANICOLAOU, G.C. 1992b Water waves in shallow channels of rapidly varying depth. *J. Fluid Mech.* **31**, 311–332.
- OGILVY, J.A. 1988 Computer simulation of acoustic wave scattering from rough surfaces. *J. Phys. D: Appl. Phys.* **21**, 260–277.
- PEREGRINE, D.H. 1967 Long waves on a beach. *J. Fluid Mech.* **27**, 815–827.
- PIHL, J.H., JØRGEN, H., MEI, C.C. & HANCOCK, M.J. 2002 Surface gravity waves over a two-dimensional random seabed. *Phys. Rev. E* **66** (1), 016611.
- PORTER, R. 2019 An extended linear shallow-water equation. *J. Fluid Mech.* **876**, 413–427.
- PORTER, R. & PORTER, D. 2003 Scattered and free waves over periodic beds. *J. Fluid Mech.* **483**, 129–163.
- ROGERS, W.E., MEYLAN, M.H. & KOHOUT, A.L. 2021 Estimates of spectral wave attenuation in antarctic sea ice, using model/ data inversion. *Cold Regions Sci. Tech.* **182**, 103198 (13 pages).
- ROGERS, W.E., THOMSON, J., SHEN, H.H., DOBLE, M.J., WADHAMS, P. & CHENG, S. 2016 Dissipation of wind waves by pancake and frazil ice in the autumn beaufort sea. *J. Geophys. Res.: Oceans* **121**.
- SARRIS, G., HASLINGER, S.G., HUTHWAITE, P., NAGY, P.B. & LOWE, M.J.S. 2021 Attenuation of rayleigh waves due to surface roughness. *J. Acoust. Soc. Am.* **149**, 4298–4308.
- SQUIRE, V.A., DUGAN, J.P., WADHAMS, P., ROTTIER, P.J. & LIU, A.J. 1995 Of ocean waves and sea. *Ann. Rev. Fluid Mech.* **27**, 115–168.
- THOMSON, J., HOŠEKOVÁ, L., MEYLAN, M.H., KOHOUT, A.L. & KUMAR, N. 2021 Spurious rollover of wave attenuation rates in sea ice caused by noise in field measurements. *J. Geophys. Res.: Oceans* **126** (3), e2020JC016606 (16 pages).
- WADHAMS, P., PARMIGGIANI, F.F., CAROLIS, G. DE, DESIDERIO, D. & DOBLE, M.J. 2004 Sar imaging of wave dispersion in antarctic pancake ice and its use in measuring ice thickness. *Geophys. Res. Lett.* **31**, L15305.
- WADHAMS, P., SQUIRE, V.A., GOODMAN, D.J., COWAN, A.M. & MOORE, S.C. 1988 The attenuation rates of ocean waves in the marginal ice zone. *J. Geophys. Res.: Oceans* **93** (C6), 6799–6818.